Experimental Study of Slat Noise from 30P30N Three-Element High-Lift Airfoil in JAXA Hard-Wall Low-Speed Wind Tunnel

Mitsuhiro Murayama[1], Kazuyuki Nakakita[2], Kazuomi Yamamoto[3], Hiroki Ura[4], and Yasushi Ito[5]
Japan Aerospace Exploration Agency, Mitaka, Tokyo, 181-0015, Japan

Meelan M. Choudhari[6]
NASA Langley Research Center, Hampton, VA 23681, USA

Aeroacoustic measurements associated with noise radiation from the leading edge slat of the canonical, unswept 30P30N three-element high-lift airfoil configuration have been obtained in a 2 m × 2 m hard-wall wind tunnel at the Japan Aerospace Exploration Agency (JAXA). Performed as part of a collaborative effort on airframe noise between JAXA and the National Aeronautics and Space Administration (NASA), the model geometry and majority of instrumentation details are identical to a NASA model with the exception of a larger span. For an angle of attack up to 10 degrees, the mean surface *Cp* distributions agree well with free-air computational fluid dynamics predictions corresponding to a corrected angle of attack. After employing suitable acoustic treatment for the brackets and end-wall effects, an approximately 2D noise source map is obtained from microphone array measurements, thus supporting the feasibility of generating a measurement database that can be used for comparison with free-air numerical simulations. Both surface pressure spectra obtained via Kulite™ transducers and the acoustic spectra derived from microphone array measurements display a mixture of a broad band component and narrow-band peaks (NBPs), both of which are most intense at the lower angles of attack and become progressively weaker as the angle of attack is increased. The NBPs exhibit a substantially higher spanwise coherence in comparison to the broadband portion of the spectrum and, hence, confirm the trends observed in previous numerical simulations. Somewhat surprisingly, measurements show that the presence of trip dots between the stagnation point and slat cusp enhances the NBP levels rather than mitigating them as found in a previous experiment.

Nomenclature

$AOAu$	=	Uncorrected (i.e., geometric) angle of attack
c	=	Stowed chord length
c_{flap}	=	Local chord length of flap
c_{main}	=	Local chord length of main wing
c_{slat}	=	Local chord length of slat
C_l	=	Lift coefficient
C_p	=	Surface pressure coefficient
CAA	=	Computational Aeroacoustics
CFD	=	Computational Fluid Dynamics
M_∞	=	Freestream Mach number
PSD	=	One sided power spectral density
PSP	=	Pressure sensitive paint
RANS	=	Reynolds Averaged Navier-Stokes
U_∞	=	Freestream velocity

[1] Associate Senior Researcher, Institute of Aeronautical Technology, 6-13-1 Osawa, Senior Member AIAA.
[2] Senior Researcher, Institute of Aeronautical Technology, 6-13-1 Osawa, Senior Member AIAA.
[3] Senior Researcher, Institute of Aeronautical Technology, 6-13-1 Osawa, Senior Member AIAA.
[4] Associate Senior Researcher, Institute of Aeronautical Technology, 6-13-1 Japan, Member AIAA.
[5] Researcher, Institute of Aeronautical Technology, 6-13-1 Osawa, Japan, Senior Member AIAA.
[6] Aerospace Technologist, Computational AeroSciences Branch, Mail Stop 128, Associate Fellow, AIAA.

x = Coordinate in the streamwise direction
y = Coordinate in the spanwise direction
α_u = Uncorrected (i.e., geometric) angle of attack

I. Introduction

Due to longstanding efforts targeting the reduction of noise associated with aircraft engines, airframe noise has become an important contributor to the overall noise, especially during approach for landing when the aircraft engines are throttled down. Therefore, technologies for airframe noise reduction have become increasingly important for the development of future civil aircraft. A leading–edge slat is commonly used as part of the high-lift devices deployed during landing and take-off, and the unsteadiness associated with flow separation within the slat cove region is known to be one of the major components of the overall airframe noise.[1-3] The shear layer emanating from the slat cusp and its subsequent reattachment upstream of the slat trailing edge lead to a primarily broadband noise spectrum. Often, however, the slat noise spectrum also exhibits narrowband peaks (NBPs) superimposed on the broadband portion, especially in the case of two-dimensional (i.e., unswept) wind tunnel configurations at lower than full-scale Reynolds numbers. The frequencies associated with the NBPs are dependent on both the configuration geometry and flow conditions such as angle of attack, flow Reynolds number, and the state of the boundary layer flow over the high lift configuration. Finally, an additional peak associated with vortex shedding behind a slat trailing edge with a finite thickness may also be observed, albeit for typical wind tunnel models the frequency of trailing edge shedding tends to be significantly higher than the dominant range of slat cove noise.[4-5]

By revealing the details of the underlying unsteady flow field and the resulting noise characteristics, high-fidelity computational investigations can greatly aid the understanding of the noise generation mechanisms and, hence, help devise low noise design concepts that can help achieve the ambitious noise reduction targets for future aircraft without any significant penalties in terms of added weight and/or aerodynamic efficiency. Due to recent progress in Computational Fluid Dynamics (CFD) technologies based on the Reynolds-Averaged Navier-Stokes (RANS) equations along with continued advances in computer resources, the accuracy of computational predictions of the steady-state aerodynamic phenomena has reached a level that makes such predictions an integral part of the aircraft design process, not only for cruise but also for the take-off and landing phases with the high-lift devices deployed.[6-8] On the other hand, routine applications of CFD and Computational Aeroacoustics (CAA) to simulate airframe noise from high-lift devices and landing gear would require further progress to address the difficulties associated with grid generation, prediction accuracy and computational resources for simulating delicate, unsteady, high-Reynolds-number flow fields over complicated geometries. In recent years, efforts to assess, validate, and improve the CFD/CAA methodologies for airframe noise computations have been promoted internationally through the AIAA series of workshops on Benchmark problems for Airframe Noise Computations (BANC).[4-5, 9]

The BANC-II Workshop, which was held in June, 2012 in Colorado Springs, Colorado, included eight problem categories representing canonical configurations related to selected aspects of airframe noise.[9] Category 7 under this workshop, which was proposed and coordinated by NASA Langley Research Center, targeted the slat noise problem in the context of the Modified-Slat 30P30N 3-Element Airfoil that corresponds to a generic, two-dimensional (i.e., unswept) high-lift configuration.[4-5] In previous work,[10] an extensive set of wind tunnel measurements was performed for the 30P30N configuration with the original slat contour, in addition to a series of computational studies based on varying levels of unsteady flow resolution.[11-12] To address the need for in-depth unsteady measurements, identified in part on the basis of these computational investigations, the slat contour was made slightly thicker along the pressure surface to allow the installation of a spanwise array of unsteady pressure transducers just ahead of the slat trailing edge. Based on RANS computations, the effect of slat contour modification on the flow field within the slat cove region and, hence, on the aeroacoustic characteristics of the model, was expected to be small. The unsteady pressure measurements using the newly designed model had not been obtained prior to the BANC-II Workshop. Thus, the purpose of category 7 in the BANC-II Workshop was to enable comparisons with other prior data as well as to provide a basis for the assessment of airframe noise simulation codes via blind comparisons with measurements that would become available after the 2012 workshop and, also, to provide guidance for those measurements.

A critical ingredient of benchmark data for airframe noise computations corresponds to in-depth near-field measurements characterizing the spatial-temporal structure of the unsteady flow along the surface and in the off-body region. Furthermore, a benchmark quality dataset must include information about the accuracy/uncertainty of each measurement. To meet these requirements, measurements using models with nominally the same geometry and an overlapping yet synergistic set of measurement techniques are being (or will be) acquired in multiple facilities including those at JAXA, Florida State University, and NASA. JAXA has accumulated the experience in the wind

tunnel tests for the slat noise.[13-19] At JAXA, the following wind tunnel measurements have been planned as part of a collaborative effort with NASA Langley Research Center to provide a portion of the dataset for Category 7 of the BANC workshops and, in general, an improved understanding and characterization of slat noise including the NBPs:

(1) Reliable near-field data from a flow field with good two-dimensionality (measurements include static and dynamic pressure at select locations, including spanwise coherence) and qualitative acoustics maps based on a phased array of microphones within a closed hard-wall test section
(2) More extensive unsteady surface pressure including spanwise coherence obtained using unsteady pressure sensitive paint (PSP)[19]
(3) Aeroacoustic measurements in JAXA's anechoic Kevlar-wall test section[17-18]

The above tests are designed to leverage on JAXA's extensive experience along with their previously established wind tunnel techniques for slat noise measurements.[13-19]

The first wind tunnel test targeting the above mentioned data under (1) and a portion of (2) was completed during April 2013 in the JAXA 2 m × 2 m (6.56 ft × 6.56 ft) Low-speed Wind Tunnel (JAXA-LWT2) with a hard-wall test section. This paper describes the basic aerodynamic and aeroacoustic measurements of the 30P30N three-element high-lift airfoil obtained during this test. An outline of the experimental setup including the model, the wind tunnel facility, and measurement strategy is given in Section II. Section III presents a summary of the data obtained and the lessons learned from this data. Concluding remarks are presented in Section IV.

II. Experimental setup

A. 30P30N Three-Element High-Lift Airfoil

Figure 1 shows the BANC-II modified-slat 30P30N three-element high-lift airfoil. The deflection angles of both the slat and the flap are equal to 30°. As mentioned in the Introduction, minor modifications were made to the pressure surface contour of the original 30P30N slat to allow the installation of unsteady pressure transducers just ahead of the slat trailing edge.

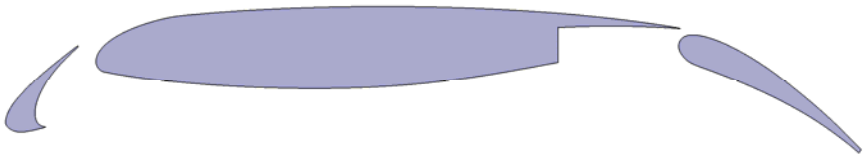

Figure. 1 Modified-slat 30P30N three-element high-lift airfoil.

B. Experimental Facilities, Models and Measurements

The JAXA-LWT2 is an atmospheric pressure, closed-circuit tunnel with a square test section of 2 m (6.56 ft) in height, 2 m in width, and 4 m (13.12 ft) in length. Measurements can be performed with either a conventional, hard-wall test section or a Kevlar-wall test section that is designed to minimize the effects of acoustic reflections from the tunnel walls. When used in conjunction with the anechoic chamber surrounding the test section, the Kevlar-wall test section enables improved acoustic measurements while eliminating the effects of jet deflection associated with the testing of high-lift models in open-jet aeroacoustic facilities. During the initial phase of research described in this paper, the JAXA-LWT2 with a closed hard-wall test section was used to obtain various measurements including both near-field data (based on static pressure taps, unsteady pressure transducers, and unsteady PSP measurements) and noise source identification via a phased-microphone array mounted on the tunnel wall facing the pressure surface of the model.

The acoustic phased array consisted of 96 microphones (B&K type 4954) distributed within a circle of 1.0 m (3.28 ft) in diameter. The microphones have a frequency range of 4 Hz to 100 kHz, and their dynamic range extends from 35 dB(A) to 165 dB(A). The A/D converters have 24 bit resolution and a maximum sampling rate of 204.8 kHz, although a sampling rate of 81.92 kHz was used in this test. The microphone array was designed for the frequency range of 0.4 kHz to 31.5 kHz. The dynamic range of this array at the center frequencies of one-third octave bands across this range was 10 dB, and the beam width at the highest design frequency (31.5 kHz) was equal to 10 mm. The noise source localization was performed using a conventional beamforming method after removing the diagonal of the cross-spectral matrix (i.e., the auto-spectra of the microphones) to reduce the influence of background noise and reflection in the closed, hard-wall test section.[20-22] Images of model and array installation in the JAXA-LWT2 are shown in Figures 2(a) and 2(b). The center of rotation of the model was set to 40% of the stowed chord in the x direction, and the center of the microphone array was also aligned with the same x location.

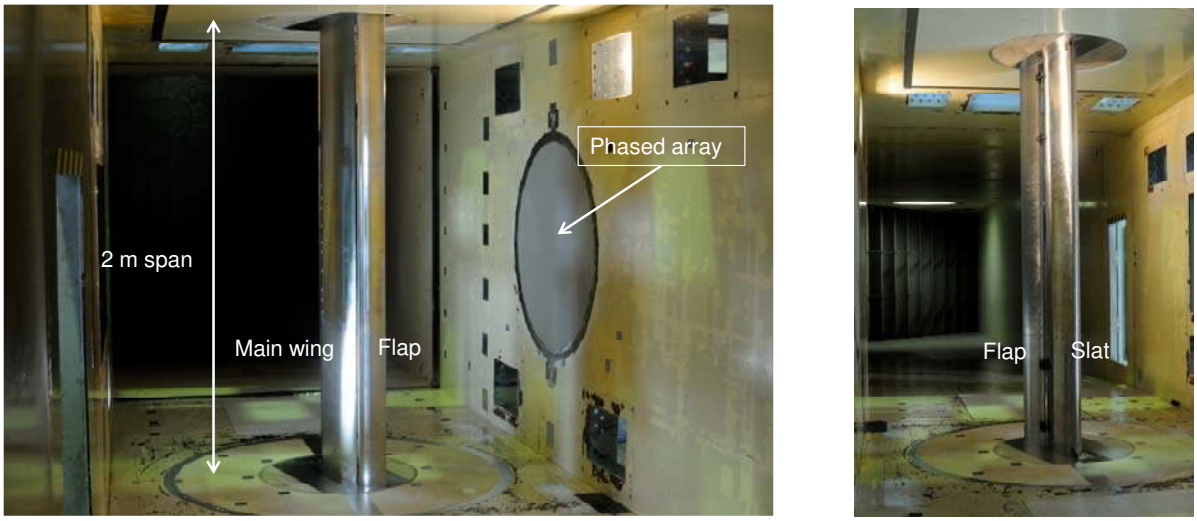

(a) Upstream view of the suction side of the model

(b) Downstream view of the pressure side of the model

Figure 2. Model mounted in the JAXA-LWT2.

The wind tunnel test in the JAXA-LWT2 used a new 30P30N two-dimensional model with the modified slat contour. The stowed chord length of the airfoil model corresponds to 0.4572 m (18 in), which is equal to that of the modified-slat configuration that is undergoing concurrent investigations in the FSU Aeroacoustics Facility as well as the original 30P30N model that was tested in the Basic Aerodynamic Research Tunnel (BART) at NASA Langley Research Center. Since the nominal (i.e., baseline) Mach number for the measurements in all three facilities is also the same ($M_\infty = 0.17$ or $U_\infty = 58$ m/s = 190.3 ft/s), the nominal flow Reynolds number ($Re_c = 1.71 \times 10^6$) is also the same across all three experiments. However, the spanwise extent of the model varies from one facility to the other, with the present model having the largest span (2.0 meters, 6.56 ft) and, hence, the highest aspect ratio (A.R. = 4.37) among all three wind tunnels. The higher aspect ratio should minimize the influence of the side walls and provide the best approximation to a nominally two-dimensional flow field. Figure 3 shows the model setup in the JAXA-LWT2. Because of larger cross-section of the JAXA-LWT2, the present wind tunnel configuration also has the lowest blockage ratio associated with model installation within the test section and, hence, also provides the closest approximation to the in-flight (i.e., free-air) configuration.

Selection of the size and location of the brackets to support the slat and the flap was driven by three objectives: maximize the two-dimensionality of the flow field within the mid-span region, minimize any changes in the slat- and flap-gap and overlap due to the aerodynamic loading, and limit the aerodynamic and aeroacoustics effects of the brackets. Figure 4 displays the bracket configuration used to support the slat and the flap. Figure 5 shows the spanwise locations of the brackets, static pressure taps, and Kulite™ unsteady pressure transducers. RANS CFD solutions of a configuration including the brackets were used to reduce both the strength of the vortical structures generated from the brackets and the influence of the bracket wakes on flow separation downstream. Figure 6 shows the surface restricted streamlines and *Cp* distribution based on the free-air 3-D RANS predictions with a single slat bracket for $\alpha = 5.5°$ and 12°. The flow separation over the flap behind the bracket is confined within the span length of $2*c_{slat}$.

Our past experience[13, 16] indicated that the junctions between the slat and the relatively thick boundary layer along the ceiling and the floor of the wind tunnel form a source of extraneous noise. To reduce this noise, the top and bottom edges of the slat were modified into aerodynamically shaped, drooped leading-edge sections extending through the thickness of the boundary layer on the wind tunnel wall. The drooped geometry filled in the slat cove and slat gap regions via a 40 mm (1.57 in) high, quasi-2D shape with 3D rounding at the corner edge. The slat brackets at both top and bottom edges of the slat are hidden inside the drooped geometries. RANS CFD computations were performed for a flow configuration that included the tunnel floor and ceiling (i.e., spanwise ends of the model), but was unconfined on the pressure and suction sides of the model. Flow visualizations from these CFD solutions based on an estimated thickness of the tunnel wall boundary layer are shown in Fig. 7 for four different configurations. Figure 7(a) corresponds to the baseline geometry without the drooped sections near the

floor and the ceiling, whereas Figs. 7(b) through 7(d) correspond to three different drooped geometries. Two of the drooped geometries involve 2D shapes of different height (20 mm (0.79 in) and 40 mm (1.57 in), respectively), whereas the third drooped geometry with 40 mm (1.57 in) height has a rounded shape near the inboard edge.

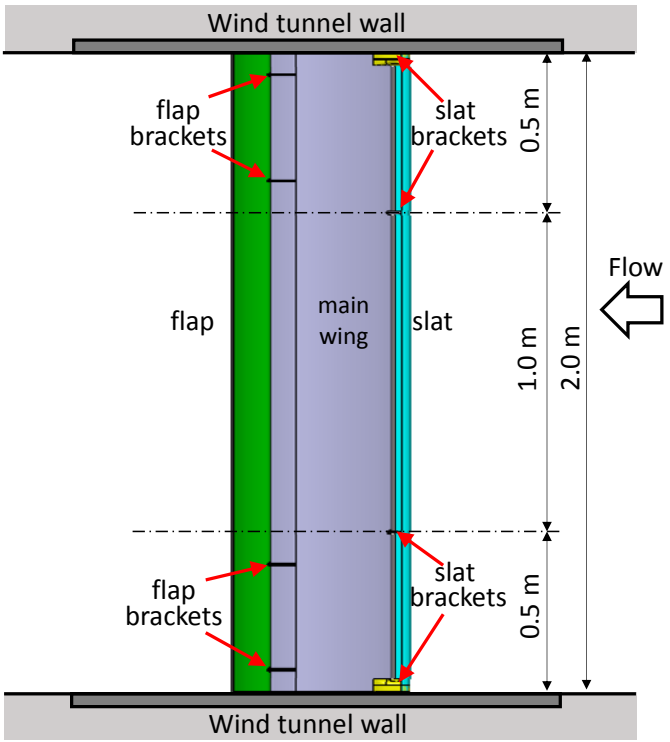

Figure 3. Model setup in the JAXA-LWT2 viewed from pressure side of the model.

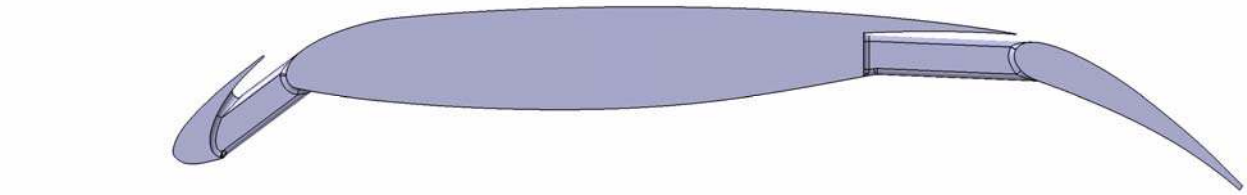

(a) Side view of brackets

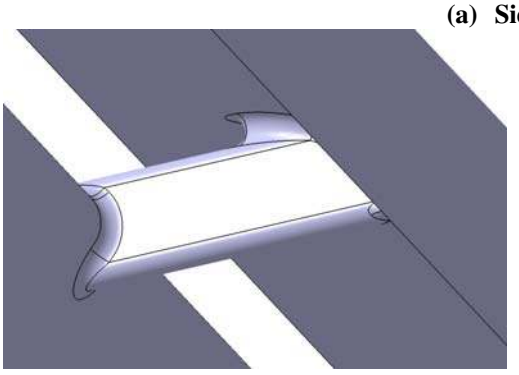

(b) Slat bracket viewed from lower side of slat

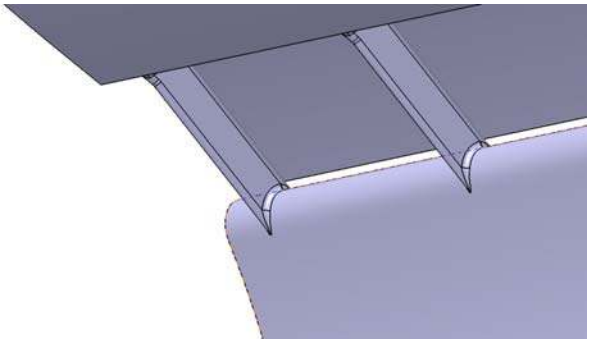

(c) Flap brackets viewed from lower side

Figure 4. Brackets to support slat and flap.

In the cases without any droop (Fig. 7(a)) and with the 20mm high droop (Fig. 7(b)), the distributions of loss of total pressure indicates that the boundary layer on the side-wall of the wind tunnel was sucked into the gap flow

between the slat and the main wing. With the taller, 40 mm high droop geometry (Fig. 7 (c)), however, the influence of the tunnel wall boundary layer on the gap flow was avoided. The rounded droop in Fig. 7(d) was designed to reduce the flow separation from the sharp corners associated with the quasi-2D droop geometries visible in Figs. 7(b) and 7(c). Moreover, to reduce the extraneous noise generated by the brackets and the slat edge, acoustic treatments in the form of furry materials were also applied in the regions surrounding the brackets of the slat and near the droops. Figure 8 shows the materials eventually selected for the wind tunnel measurements following several trials. The furry materials with a height of 6 mm (0.236 in) were put on the slat cove behind the slat brackets and near the drooped sections at the floor and ceiling of the test model, as well as both sides of the brackets as shown in Fig. 8. No acoustic treatment was applied to the flap brackets or at the side-walls of the flap because any extraneous noise contributions from those regions were lower than those from slat and the slat brackets on the noise source maps.

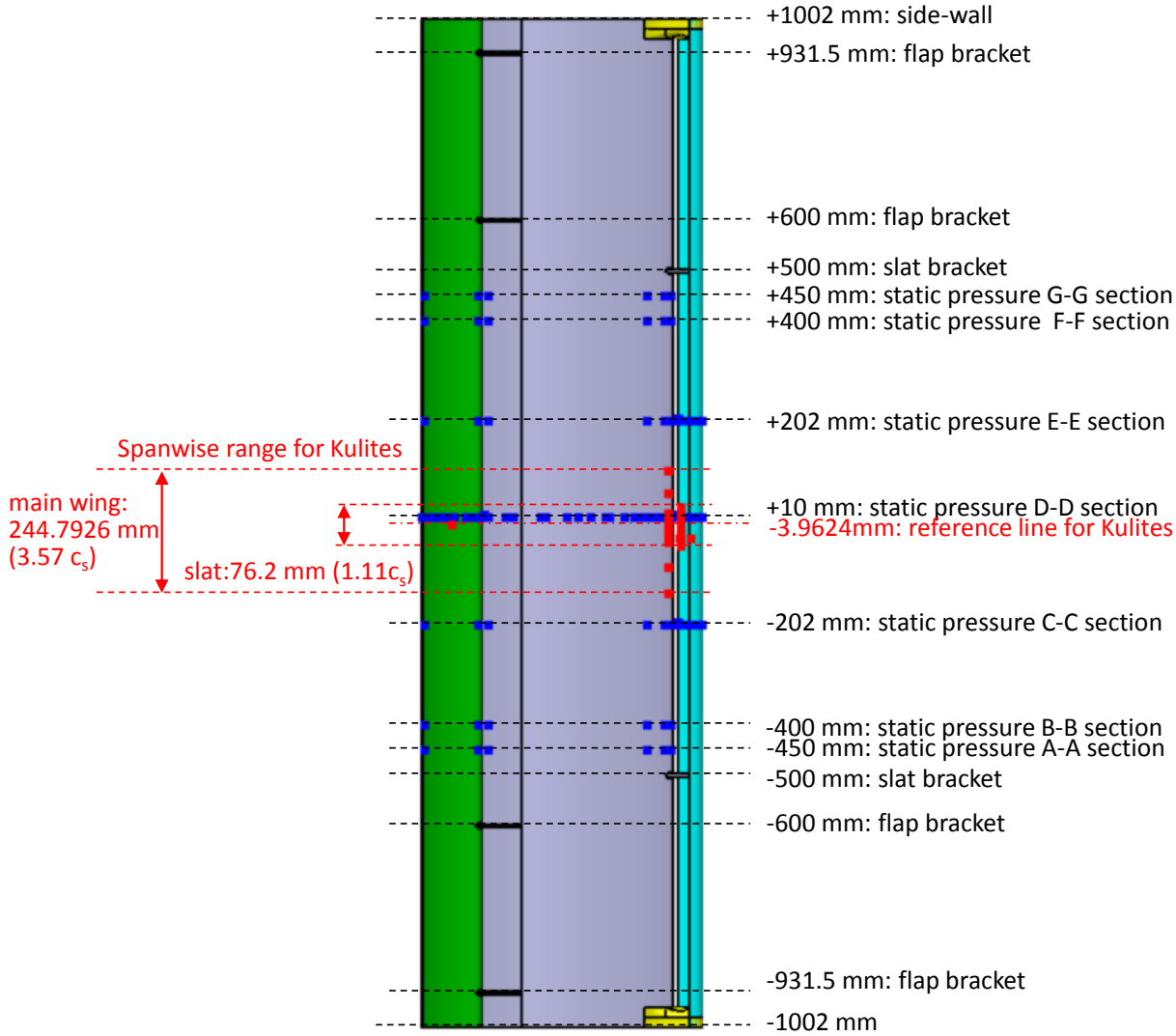

Figure 5. Locations of slat/flap brackets, static pressure taps (blue) and Kulite™ unsteady pressure transducers (red).

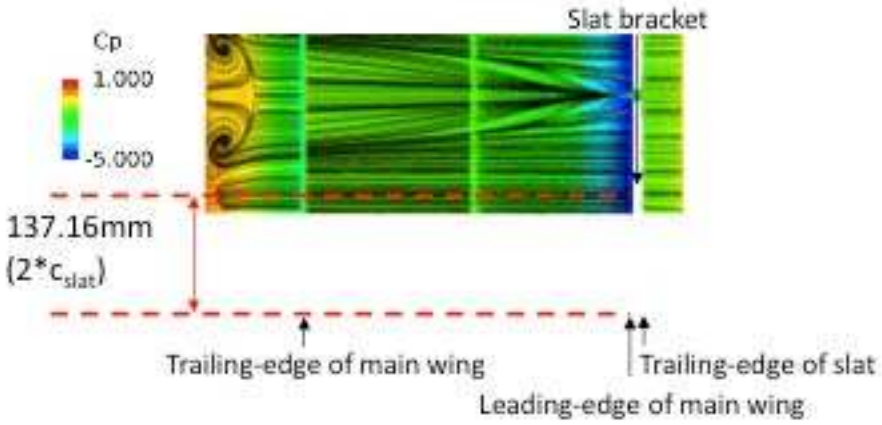

(a) $\alpha = 5.5°$

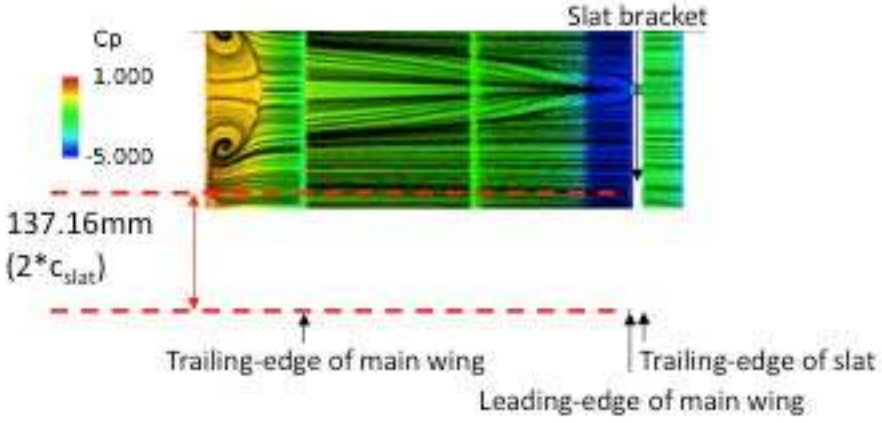

(b) $\alpha = 12°$

Figure 6. Surface restricted streamlines and *Cp* distribution viewed from suction side. Results based on the 3-D RANS predictions incorporating slat brackets. Flow is from right to left.

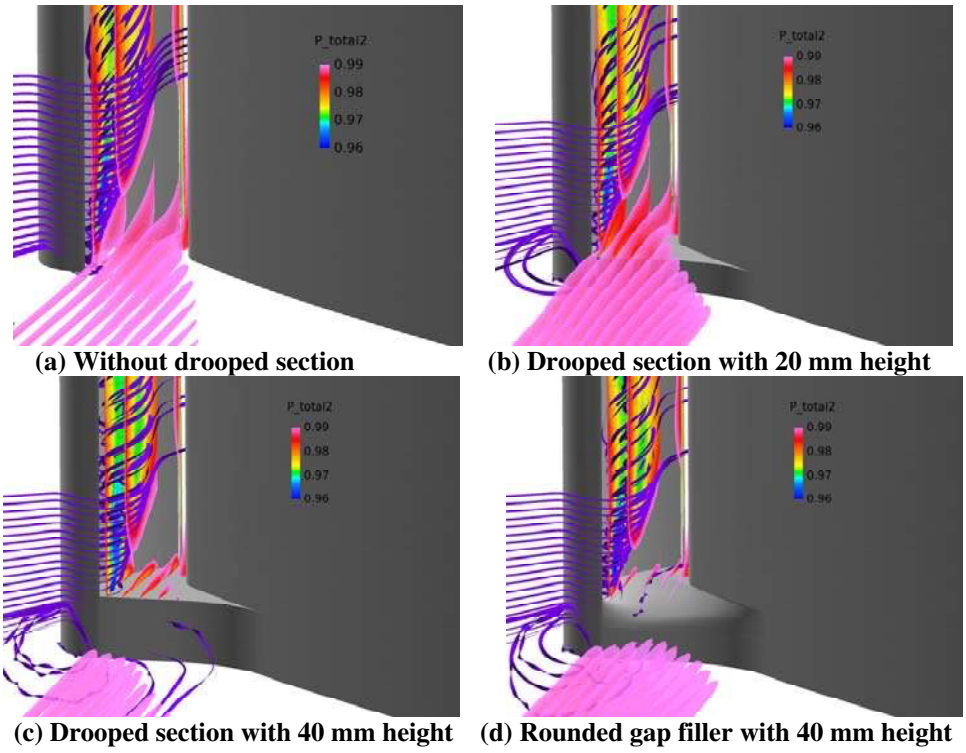

(a) Without drooped section **(b) Drooped section with 20 mm height**

(c) Drooped section with 40 mm height **(d) Rounded gap filler with 40 mm height**

Figure 7. 3-D RANS solution streamlines (purple) and total pressure distribution near the junction between the slat and the side-wall of the wind tunnel viewed from lower side of slat.

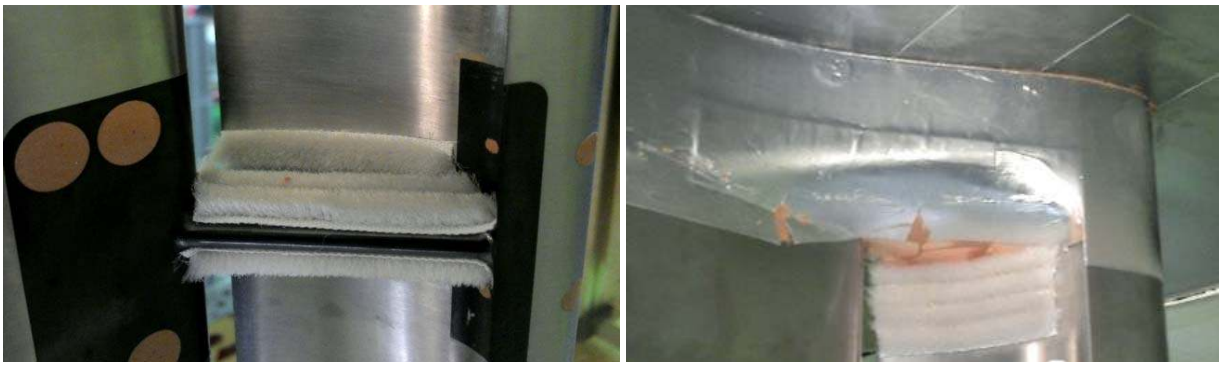

(a) Slat bracket **(b) Junction between the slat and the ceiling**

Figure 8. Acoustic treatment in the form of furry, sound absorbing materials to reduce the noise from the slat brackets and the junctions between the slat and the ceiling of the wind tunnel.

Figure 9 shows an illustrative noise source map for f = 8 kHz at U_∞ = 58 m/s (190.3 ft/s) and α_u = 0°. As seen later, this frequency falls within the primarily broadband segment of the frequency spectrum corresponding to the radiated acoustic field (i.e., the segment where no significant NBPs are observed). The pressure side of the model is shown and the free-stream direction is from the right to the left of the map. The origin of the coordinate system in these maps corresponds to the center of rotation for the model. The noise source maps are shown at one-third octave bands and in terms of sound pressure level (SPL). The microphone data was processed with a frequency bin width of 10 Hz, and then the beamforming output was combined into the one-third octave bands. The apparent noise source regions away from the model surface correspond to the side lobes resulting from the beamforming process and are not physical. As shown in Fig. 9, the overall domain used for the integration of spectra was divided into several subdomains (five subdomains each in the vicinity of the slat and the flap, respectively) so as to allow one to isolate

the contributions associated with the noise sources near the side-wall as well as the brackets on the slat and the flap. The coordinates of the integration subdomains are summarized in Table 1. Even though noise source regions with intensities of up to 20 dB below the maximum are plotted in the figure, the integration process was actually limited to regions of up to 10 dB from the maximum in order to reduce the influence of the side lobes observed in the map shown in Fig. 9. The noise source maps were computed on a planar grid with 301 points each in the chordwise and spanwise directions, respectively, while 8,192 data points uniformly spaced over a time interval of 0.1 sec with 500 averages were used for computing each FFT.

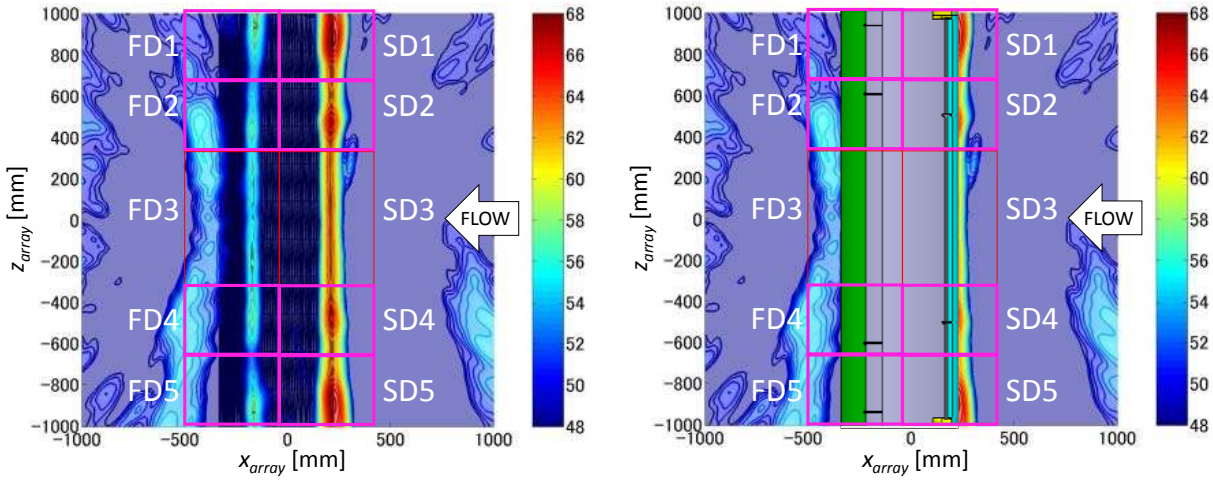

(a) Noise source map

(b) Noise source map superimposed on the model geometry

Figure 9. A sample of noise source map contours and the domains in the maps used for integration to obtain spectra. Contours are for 8 kHz sources with flow conditions U_∞ = 58 m/s and α_u = 0. Flow is from right to left.

Table 1. Coordinates of the domains for the integration of spectra in the noise source maps.

Name	x_{array} [mm]		y_{array} [mm]	
	min.	max.	min.	max.
SD 1	0	500	663.5	1002.0
SD 2	0	500	325.0	663.5
SD 3	0	500	-325.0	325.0
SD 4	0	500	-663.5	-325.0
SD 5	0	500	-1002.0	-663.5
FD 1	-500	0	663.5	1002.0
FD 2	-500	0	325.0	663.5
FD 3	-500	0	-325.0	325.0
FD 4	-500	0	-663.5	-325.0
FD 5	-500	0	-1002.0	-663.5

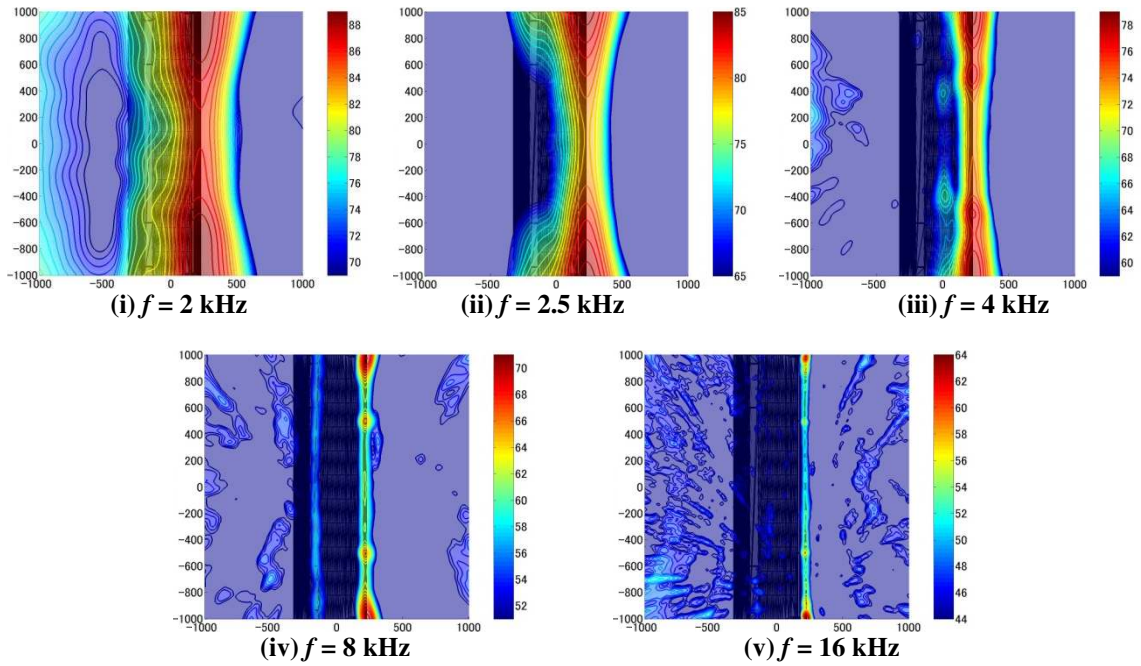

(a) α_u = 5.0°

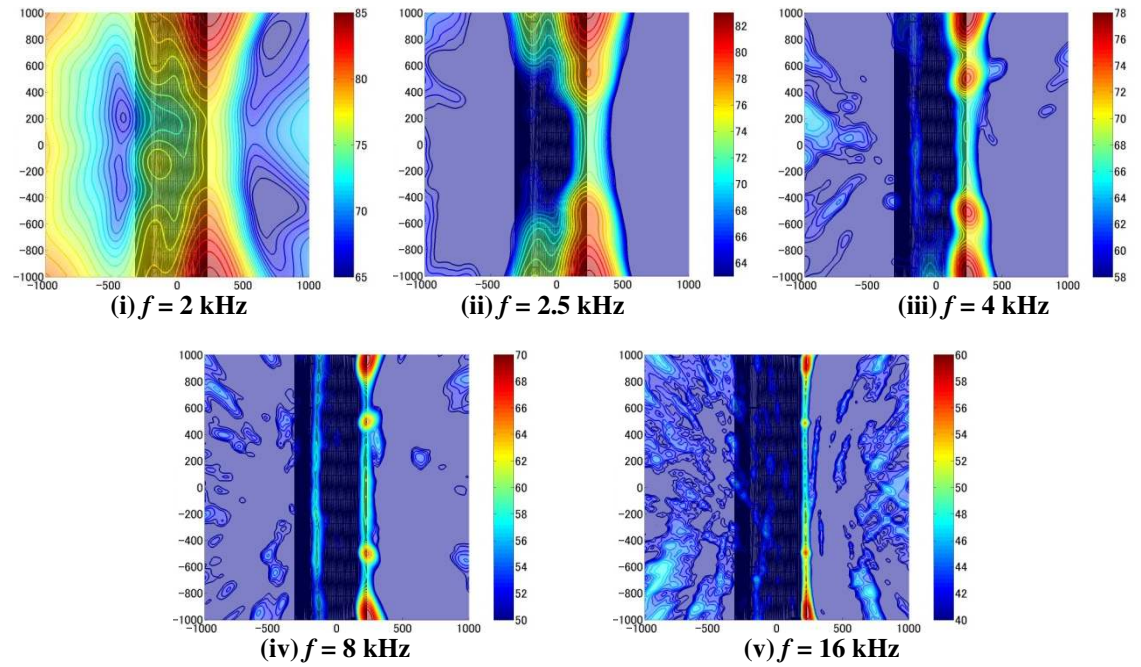

(b) α_u = 10.0°

Figure 10. Noise source maps generated by a phased-microphone array for the model configuration without any acoustic treatments around the slat brackets and the junctions between the slat and the side-wall of the wind tunnel (U_∞ = 58 m/s).

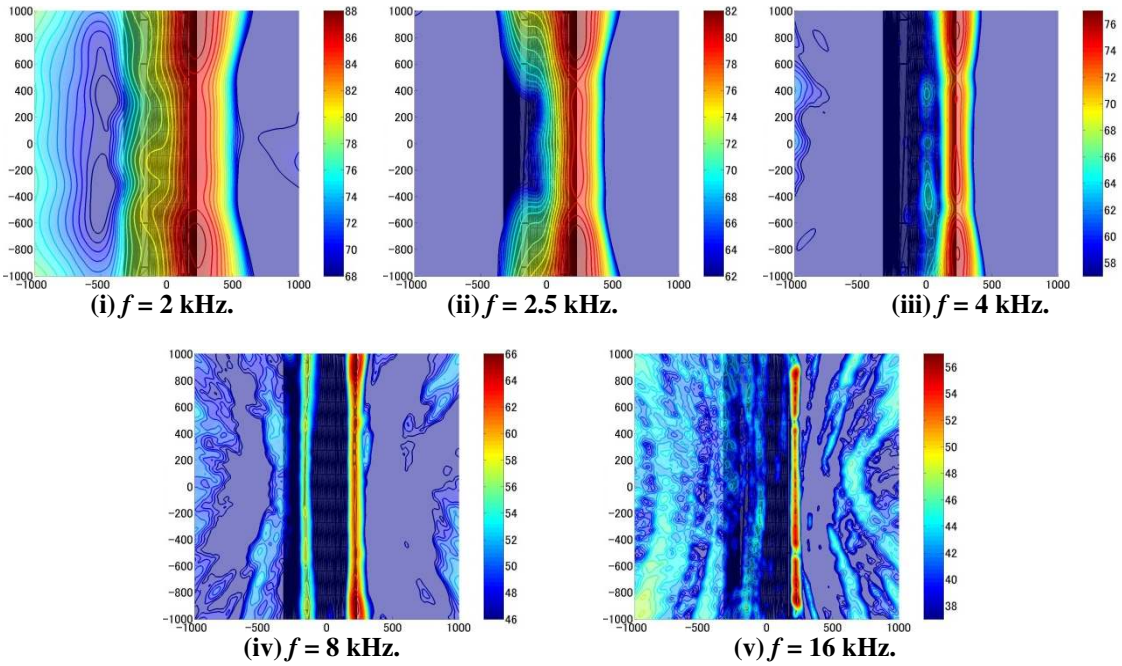

Figure. 11 Noise source maps generated by a phased-microphone array on the configuration with acoustic treatments around the slat brackets and the junctions between the slat and the side wall of the wind tunnel (U_∞ = 58 m/s).

Figures 10 and 11 display the noise source maps obtained without and with the acoustic treatments around the slat droop and slat brackets at α_u = 5° (Figs. 10(a) and 11(a), respectively) and 10° (Figs. 10(b) and 11(b)). The noise spectra integrated over subdomains SD1, SD2, and SD3 are plotted in Figs. 12(a) – 12(c). The positions of discrete peaks within these noise spectra confirm that the noise source maps illustrate the source distributions at frequencies

that are close to those peaks, in between the peaks, and within the broad-band portion of the spectrum at higher frequencies than the NBPs (but below the high frequency lobe near 20 – 30 kHz, which corresponds to vortex shedding from the slat trailing edge). Note that the various gaps within these spectra are associated with the integration cutoff at 10 dB below the overall maximum in the noise source maps. Figure 10 clearly highlights the contributions from the extraneous noise sources from the slat brackets as well as from both ends of the slat. The acoustic treatments from Fig. 8 successfully reduced the peak noise levels resulting from the brackets and the side-edges, thereby enabling the nearly two-dimensional noise sources from the slat itself to be observed in Figure 11. The noise sources from the cove underneath the aft portion of the main wing may also be seen in Figs. 11(a)(iv), 11(b)(iv), and 11(b)(v) . The comparison of the spectra in Fig. 12 indicates that the treatment for the slat side-edges was effective especially below 8 kHz and above 16 kHz, and the extent of the noise reduction was significantly greater at α_u = 10° in comparison with that at α_u = 5°. The treatment for the brackets of the slat was also effective and the amount of the reduction was larger than that for the slat side-edges. Figure 12(c) compares the spectra integrated over subdomain SD3 within the mid-span region of the slat, which is the domain of primary relevance for slat noise measurements without end wall effects. The spectra are presented in terms of SPL with a frequency bin width of 10 Hz. Without any treatment, the spectra at α_u = 5° in the frequency ranges around 6 – 12.6 kHz and 15 – 21 kHz were excessively oscillatory and significantly lower than the corresponding spectrum with the acoustic treatment in place. Similarly, at α_u = 10°, the spectra without any acoustic treatment were too oscillatory to be useful. The dropouts and oscillatory behavior are an artifact of the array beamform map integration method. Because the integration only includes sources within 10 dB of the peak, an intense but very localized source can integrate to a small value compared with the integration of sources 10 dB lower but covering a much larger error. Sources 10 dB below the peak are excluded because errors in the conventional beamforming process typically overwhelm the solution when sources are much lower in amplitude than the peak value. More advanced deconvolution beamforming techniques can significantly reduce these errors so that an arbitrary cutoff in the integration is not needed.

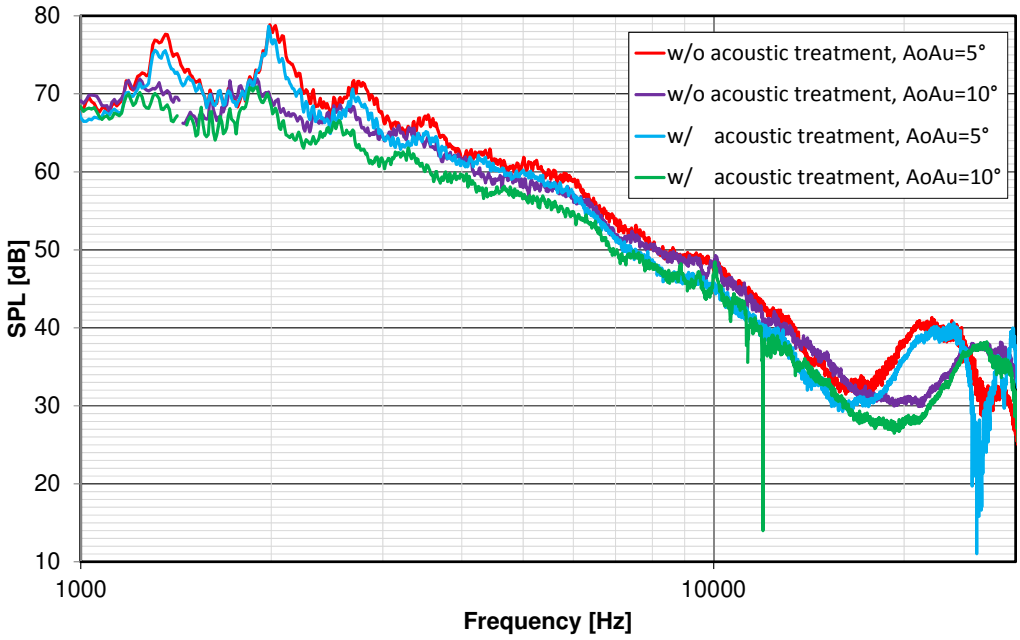

Figure 12(a) SD1

Figure. 12 Comparison of integrated spectra on the domain around the junction between the slat and the ceiling of the wind tunnel, SD1, around the slat brackets, SD2, and within the mid-span region of the slat, SD3 (U_∞ = 58 m/s, spectral bin width = 10 Hz) (continued).

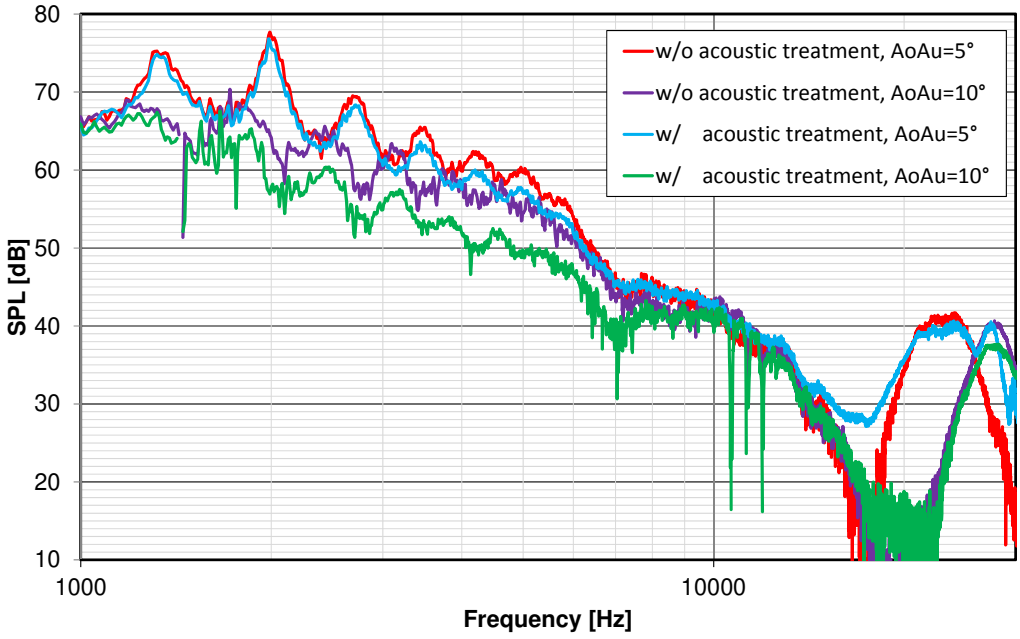

(b) SD2

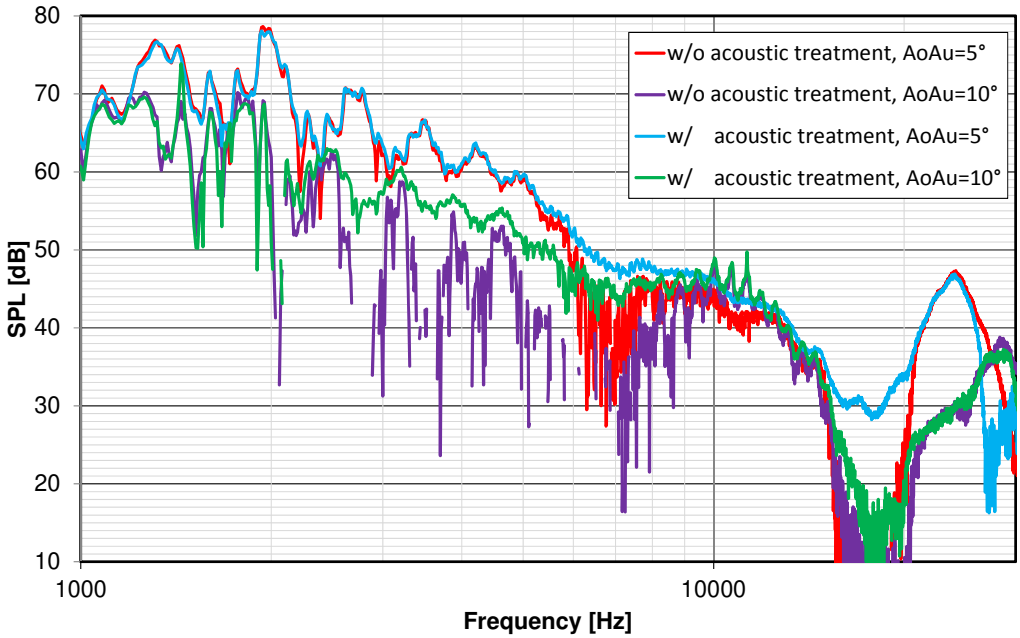

(c) SD3

Figure 12. Comparison of integrated spectra on the domain around the junction between the slat and the ceiling of the wind tunnel, SD1, around the slat brackets, SD2, and within the mid-span region of the slat, SD3 (U_∞ = 58 m/s, spectral bin width = 10 Hz) (concluded).

Unsteady pressure measurements were obtained on all three elements of the high-lift configuration, namely, the slat, main wing, and the flap. Unsteady PSP measurements for the model surfaces of the slat cove and near the leading-edge of the main wing were also obtained during the present test campaign; however, only the Kulite™ data are presented in this paper. Specifications of these transducer units are provided in Table 2 and Fig 13. The overall region spanned by the Kulite™ pressure transducers is indicated in Fig. 5.

Table 2. Detailed information about Kulite™ pressure transducers.
(Gray background identifies damaged Kulite™ pressure transducers and the (X, Z) coordinates are aligned with streamwise and spanwise directions, respectively.)

	No.	X [mm]	Z [mm]	Range [PSI]	Type
Slat	S1	2.653	-20.625	5	LQ062-(13 TO 17) PSIA
	S2	2.653	-7.137	5	LQ062-5SG
	S3	2.653	-3.962	5	LQ062-5SG
	S4	2.653	-1.700	5	LQ062-5SG
	S5	2.653	0.000	5	LQ062-5SG
	S6	2.653	2.388	5	LQ062-5SG
	S7	2.653	4.775	5	LQ062-5SG
	S8	2.653	17.475	5	LQ062-5SG
	S9	2.653	30.175	5	LQ062-(13 TO 17) PSIA
	S10	-15.900	-31.598	5	LQ062-5SG (2.1m cable)
	S11	2.653	-31.598	5	LQ062-(13 TO 17) PSIA
	S12	5.268	-31.598	5	LQ062-(13 TO 17) PSIA
	S13	2.962	-31.598	5	LQ062-5SG
	S14	2.653	-46.025	5	LQ062-(13 TO 17) PSIA
Main wing	M1	29.518	-141.599	5	XCQ062-5SG-0.1"
	M2	29.518	-88.900	5	XCQ062-5SG-0.1"
	M3	29.518	-38.100	5	XCQ062-5SG-0.1"
	M4	29.518	-20.625	5	XCQ062-5SG-0.1"
	M5	29.518	-10.312	5	XCQ062-5SG-0.1"
	M6	29.518	-6.350	5	XCQ062-5SG-0.1"
	M7	29.518	-3.962	5	XCQ062-5SG-0.1"
	M8	29.518	0.000	5	XCQ062-5SG-0.1"
	M9	29.518	4.775	5	XCQ062-5SG-0.1"
	M10	29.518	17.475	5	XCQ062-5SG-0.1"
	M11	29.518	58.115	5	XCQ062-5SG-0.1"
	M12	29.518	103.194	5	XCQ062-5SG-0.1"
Flap	F1	457.959	-3.962	5	XCQ062-5SG-0.1"

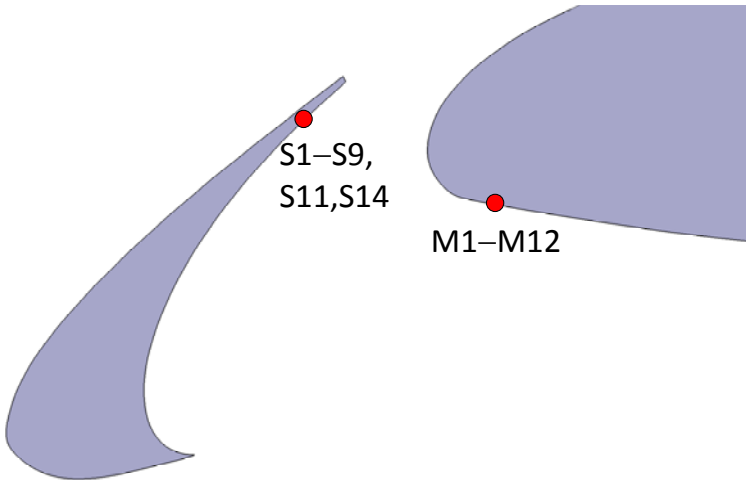

(a) Locations of spanwise arrays of Kulite™ transducers

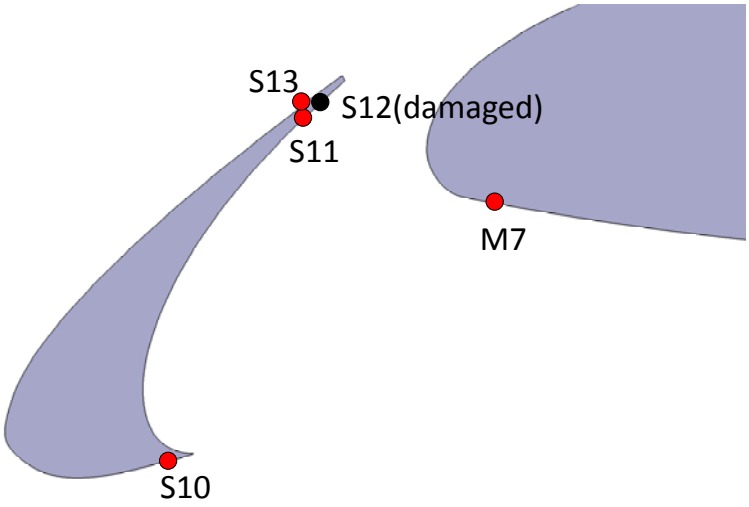

(b) Chordwise array of Kulite™ transducers along the slat and main wing at *z*= -31.5976

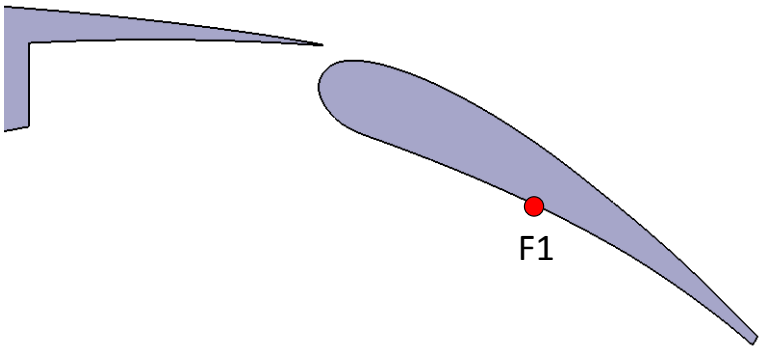

(c) Kulite™ location on the flap

Figure 13. Unsteady pressure transducer locations.

As seen from Table 2, Kulite™ transducers LQ-062-5SGs were installed within a narrow slot on the surface of the slat, and the gaps between the transducers and the model were filled with a paste. Additionally, Kulite™ transducers XCQ-062-5SG-0.1" (i.e., a special version of the XCQ-062-5SG transducers with a length equal to 0.1 inches) which were flush-mounted on the surface of the main wing and the flap. The diameter of the pressure sensing area was 1.6 mm. The data from the Kulite™ pressure transducers was sampled at 81.92 kHz following a 40 kHz low-pass-filter for anti-aliasing. The above sampling rate was the identical to that used for the microphone array measurement. The pressure transducers were calibrated in situ by using a pressure calibrator. The calibrated sensitivities were used for reducing the data obtained using the XCQ-062-5SG-0.1" sensors. However, the original sensitivities given by the manufacturer were used for LQ-062-5SGs because the installation method of the transducers was not suitable for in situ calibration using the pressure calibrator and caused a non-negligible variation in the repeatability of the calibration. A total of fourteen Kulites™ were installed on the surface of the slat, of which four transducers were aligned along the chord-wise direction and eleven transducers were aligned along the spanwise direction. Unfortunately, Kulites™ S6, S9, S12 and S14 (shown in Table 2 with a gray background) were damaged; and, therefore, the data from those are not available. Twelve Kulites™ were aligned on the lower surface of the main wing at x/c_{main} = 0.025 in the span-wise direction. A single Kulite™ was installed on the lower surface of the flap at x/c_{flap} = 0.5.

During the test, a tonal noise peak at around 1.6 kHz was found near the cove of the main wing via noise source maps and was subsequently removed by using trip dots with 0.290 mm height on the lower surface of the main wing at x/c_{main} = 0.2. The diameter of the dots was equal to 1.27 mm and the spacing between the centers of each pair of adjacent dots was equal to 2.54 mm. Figure 14 shows the trip dots on the lower surface of the main wing. Figures 15 and 16 compare both the noise source maps at 1.6 kHz and the integrated spectra within the mid-span region of the flap, FD3, for a flow condition of U_∞ = 58 m/s (190.29 ft/s) and α_u = 10°. The spectra are excessively oscillatory and, as mentioned previously, include multiple gap regions because the cut-off for the integration was set to 10 dB from the maximum level in the map, and the noise level of the main cove was much lower than that of the slat cove. Yet, the figures clearly indicate the presence of the tonal peak around 1.6 kHz near the main cove and its mitigation by the trip dots. The reader may note that the comparisons of the effectiveness of the acoustic treatments for the brackets and the spanwise edges of slat in Figs. 10, 11, and 12 were conducted without any boundary layer trip. To make the evaluation of slat noise easier, the configuration with boundary layer tripping only on the lower surface main wing at x/c_{main} = 0.2 was selected as the baseline setting discussed hereafter in this paper.

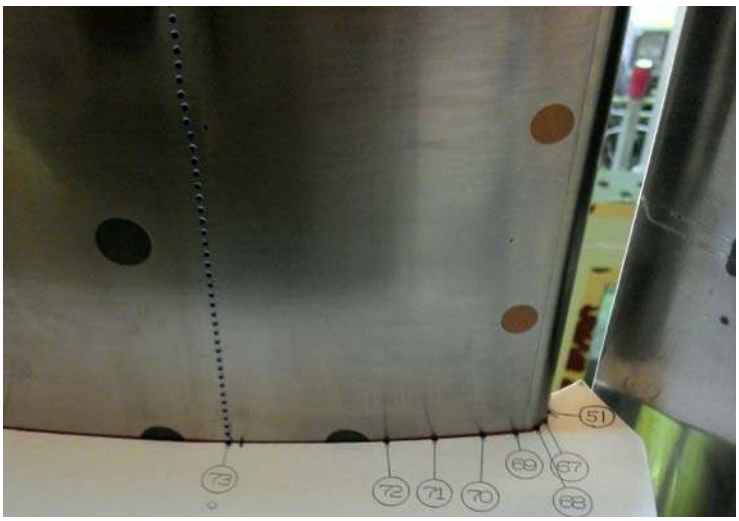

Figure 14. Trip dots on the lower surface of the main wing at x/c_{main} = 0.2. The array of dots is labeled as 73 in the figure. The height of the dots is 0.290 mm, the diameter of the dots is 1.27 mm and the spacing between the centers of each pair of adjacent dots is equal to 2.54 mm.

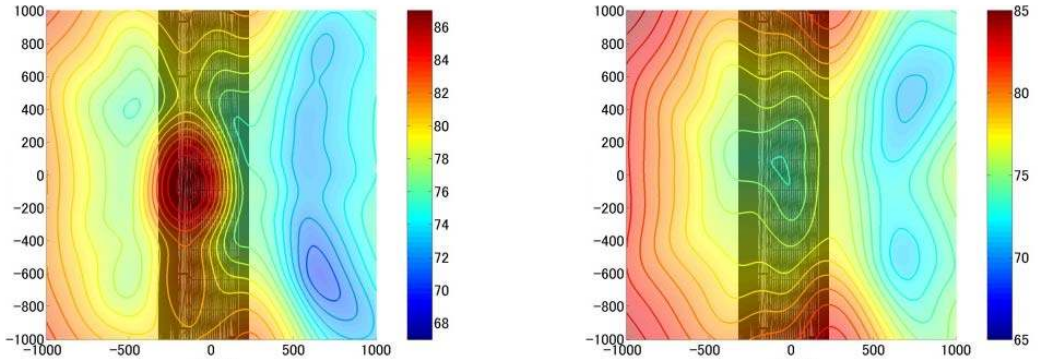

(a) Without trip dots **(b) With trip dots**

Figure 15. Illustration of the effect of trip dots on the lower surface of the main wing on noise maps (f = 1.6 kHz). The trip dots are installed at x/c_{main} = 0.2 and the flow conditions correspond to U_∞ = 58 m/s and α_u = 10°.

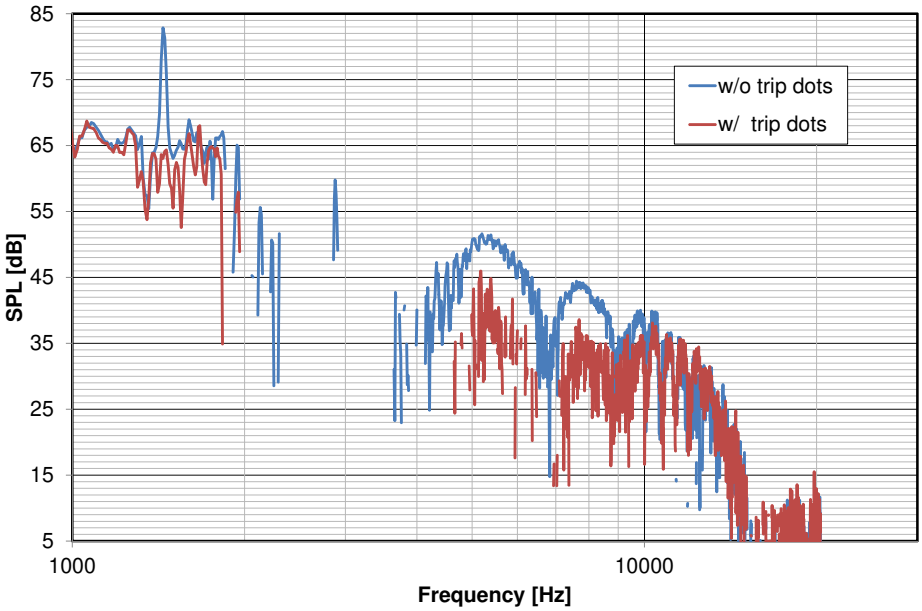

Figure 16. Effect of trip dots on the lower surface of the main wing (x/c_{main} = 0.2) on the acoustic source spectra integrated over subdomain FD3 that encompasses the mid-span region of the flap (U_∞ = 58 m/s, α_u = 10°, spectral bin width = 10 Hz).

III. Results

A. Basic Aerodynamic Characteristics

Figure 17 shows the comparison between C_l-α curves obtained, respectively, from two-dimensional steady-state RANS CFD for a free-air configuration and the measurements using the wind tunnel model. In the wind tunnel test, C_l was calculated by applying the trapezoidal integration rule to the Cp measurements obtained along the center row of pressure taps (Section D-D in Fig. 5). Two different C_l-α curves based on the CFD data are included in the figure, one obtained by applying the trapezoidal rule to the denser distribution of surface grid points in the CFD mesh and the other based on the sparser set corresponding to pressure tap locations in the experiment. The C_l value calculated using the CFD data at the pressure tap locations tend to be lower than the more accurate value based on the actual CFD mesh. The difference between the two CFD results tends to get larger with an increasing angle of attack. To enable a consistent comparison with the measured data, the lift coefficient predictions based on the same set of locations will be used in this section. The C_l-α curves based on CFD and wind tunnel measurement show reasonable

agreement with each other for $\alpha < 14°$, with the experimental curve shifted to the right by approximately 0.5° over this entire range.

Figure 18 shows the comparison between *Cp* distributions obtained from CFD and wind tunnel measurements at selected angles of attack. The CFD results show somewhat less flow separation near the trailing edge of the flap. This comparison confirms that the approximately 0.5° shift in α between the CFD and wind tunnel results also yields a good agreement between both sets of results. Accordingly, computational predictions for α = -0.5°, 3°, 5.5°, 8.5°, and 9.5° are approximately aligned with wind tunnel measurements at α = 0°, 3.5°, 6°, 9°, and 10°, respectively.

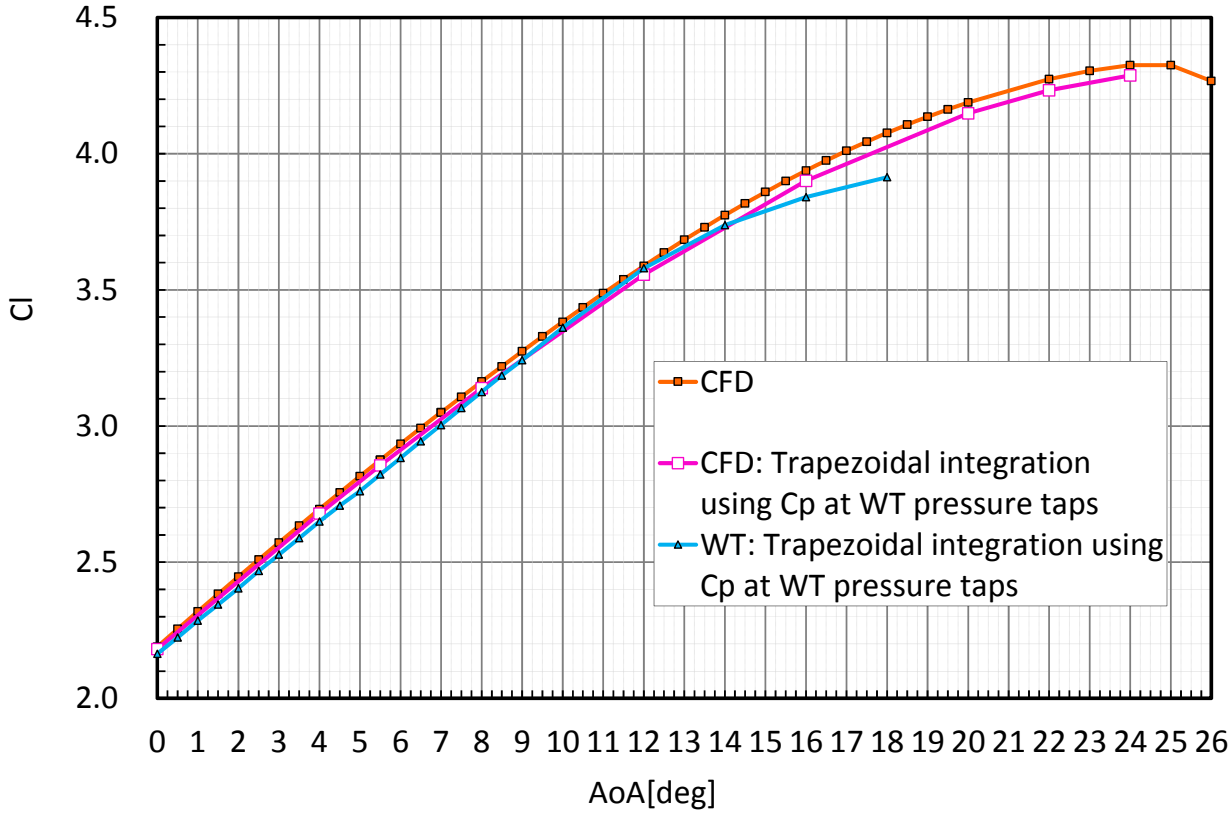

Figure 17. Comparisons of C_l-α curves based on two-dimensional steady-state RANS CFD and wind tunnel measurement.

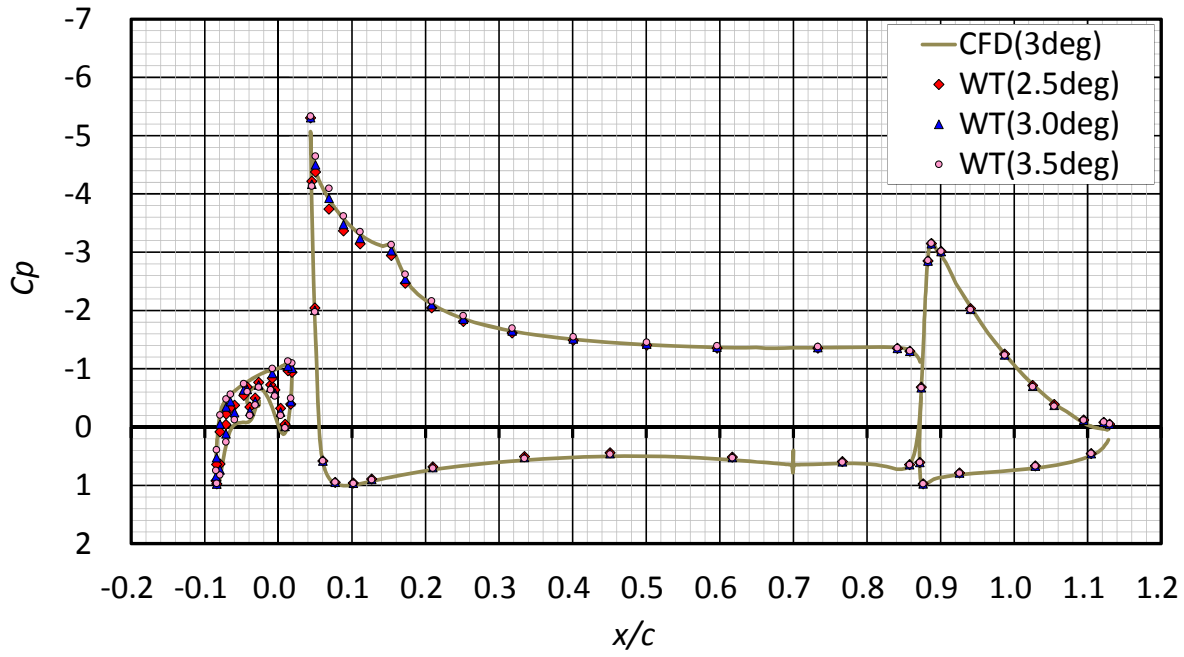

(a) $\alpha = 3°$

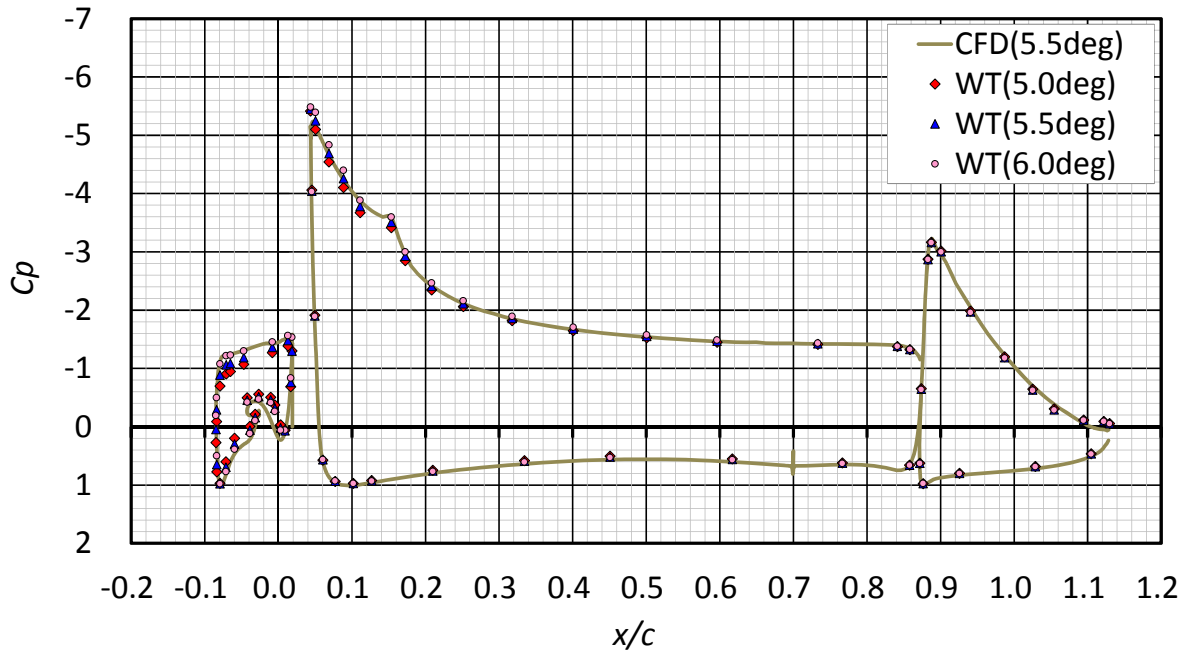

(b) $\alpha = 5.5°$

Figure 18. Comparison of mean *Cp* distributions obtained from 2D RANS computations for a free-flight configuration at a specified angle of attack α and the wind tunnel measurements at multiple, neighboring values of α. (continued)

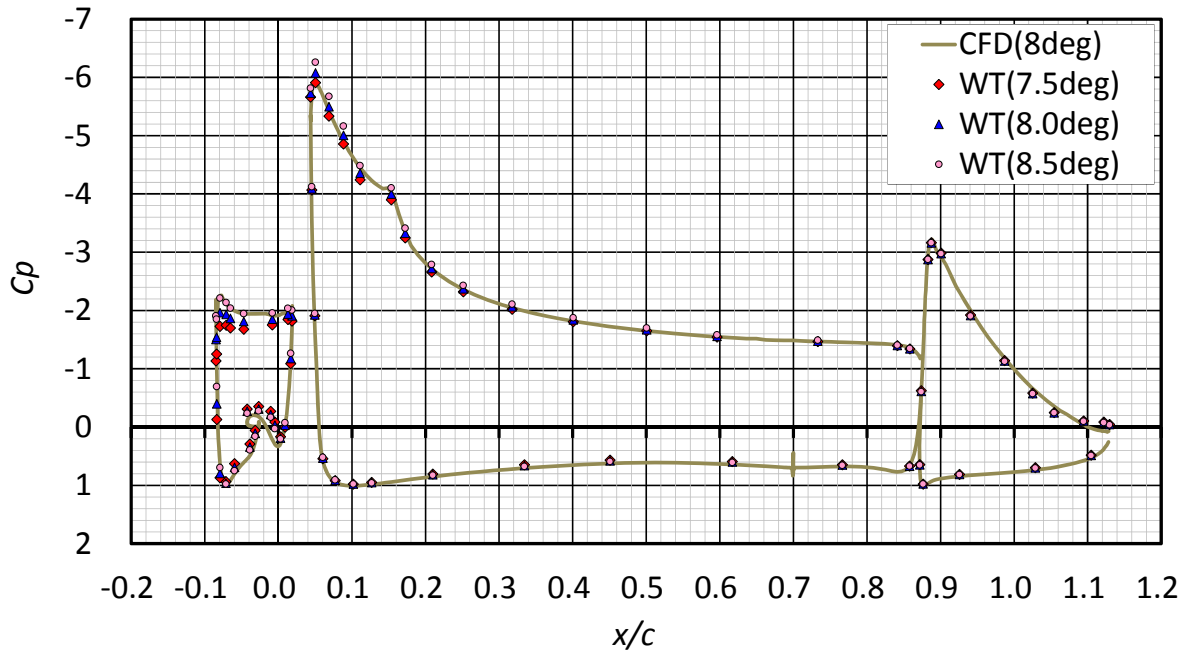

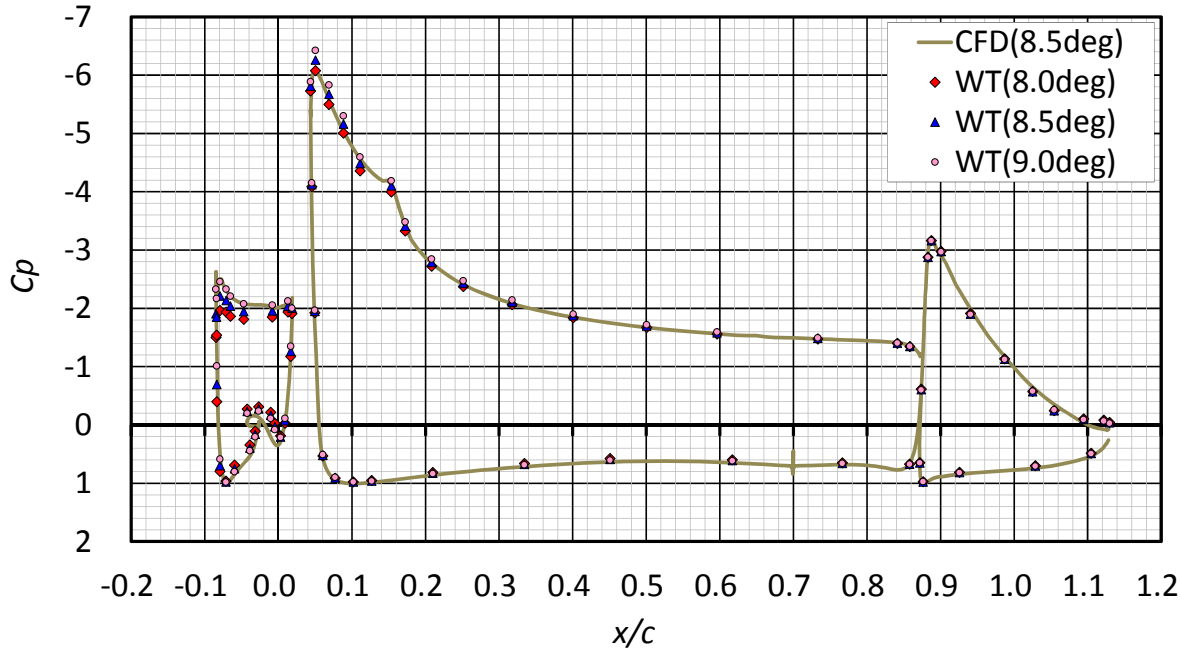

(c) $\alpha = 8.5°$

Figure 18. Comparison of mean *Cp* distributions obtained from 2D RANS computations for a free-flight configuration at a specified angle of attack α and the wind tunnel measurements at multiple, neighboring values of α. (concluded)

B. Basic Aeroacoustic Characteristics at $U_\infty = 58$ m/s

Figures 19—21 compare noise source maps identified using phased-microphone array measurements at $\alpha_u = 3.5°$, 6°, and 10°. The range of the color bar is 20 dB from the maximum in each figure. Although noise sources with relatively high SPL were found near the side-wall and around slat brackets, especially at the higher angles of attack, source maps for slat noise sources indicate good two-dimensionality within the mid-span region SD3 of -325 mm <

span < +325 mm even at $\alpha_u = 10°$. At $f = 8$ kHz and 10 kHz, noise sources from the main cove region also become visible, but the level is considerably lower than that of the slat cove noise.

Figure 22 compares the frequency spectra obtained for different angles of attack by integrating the noise source maps over the S3D domain. Figures 23(a)-(f) compare the power spectral density (PSD) of *Cp* fluctuations on the surface obtained at selected angles of attack and a fixed tunnel flow speed of $U_\infty = 58$ m/s. The selected surface locations correspond to the S3 Kulite™ pressure transducer (which is subsequently used as the reference transducer to calculate spanwise the coherence distribution) and the rest of the transducers from the chordwise array of Kulites™ along the slat (S10, S11, S13), the main wing (M7), and the flap (F1) at the fixed spanwise location of $z = -31.5976$ mm. Later, the Kulite™ transducer M7 is used as the reference transducer to calculate the spanwise coherence distribution over the leading edge of the main wing. Observe that the spectral amplitudes at the location of the flap transducer F1 are much lower than those at the slat and the main-wing transducers. NBPs of slat noise are found both in the phased array spectra in Fig. 22 and the near-field spectra in Fig. 23, and, furthermore, the peak frequencies from both sets of measurements are in good agreement as seen from Fig. 24. Although not shown, the measured range of non-dimensional frequencies (normalized by the slat chord and free-stream speed) is similar to that noted earlier for a 2-element airfoil configuration with no flap.[23] The NBPs are strongest at the lower angles of attack. An increasing angle of attack leads to progressively decreasing levels of both the broadband spectrum and the NBPs superposed thereupon. The amplitudes of the NBPs relative to the broadband spectrum are dependent on the location of the probe. Due to the highly energetic broadband hydrodynamic fluctuations associated with the impingement of unsteady structures near the reattachment location of the slat cove shear layer (sensors S3 and S11 in Figs. 23(a) and 23(c), respectively), the NBPs are barely visible above the broadband spectrum at this chordwise location. However, the sensors away from the region of vortical fluctuations (sensors S10, S13, and M7 in Fig. 23(b), 23(d), and 23(e)), the NBPs are observed more clearly. The NBPs are also visible along the lower surface of the flap as seen from the spectrum at sensor F1 in Fig. 23(f). The above observations are generally consistent with the computational findings reported earlier.[11]

Figure 23 also indicates that, contrary to the trend for both broadband and narrow-band portions of the unsteady pressure spectra associated with the slat cove unsteadiness, the strength of trailing edge shedding increases with the angle of attack, except for $\alpha_u = 10°$. The peak frequency associated with this shedding progressively shifts to a higher frequency (sensors S13 and M7 in Fig. 23 (d) and 23 (e)). At $\alpha_u = 10°$, the spectrum at sensor S13 exhibits two additional peaks between the frequency range of 7 kHz and 18 kHz as seen from Fig. 23(d). The reason behind these two peaks remains to be ascertained.

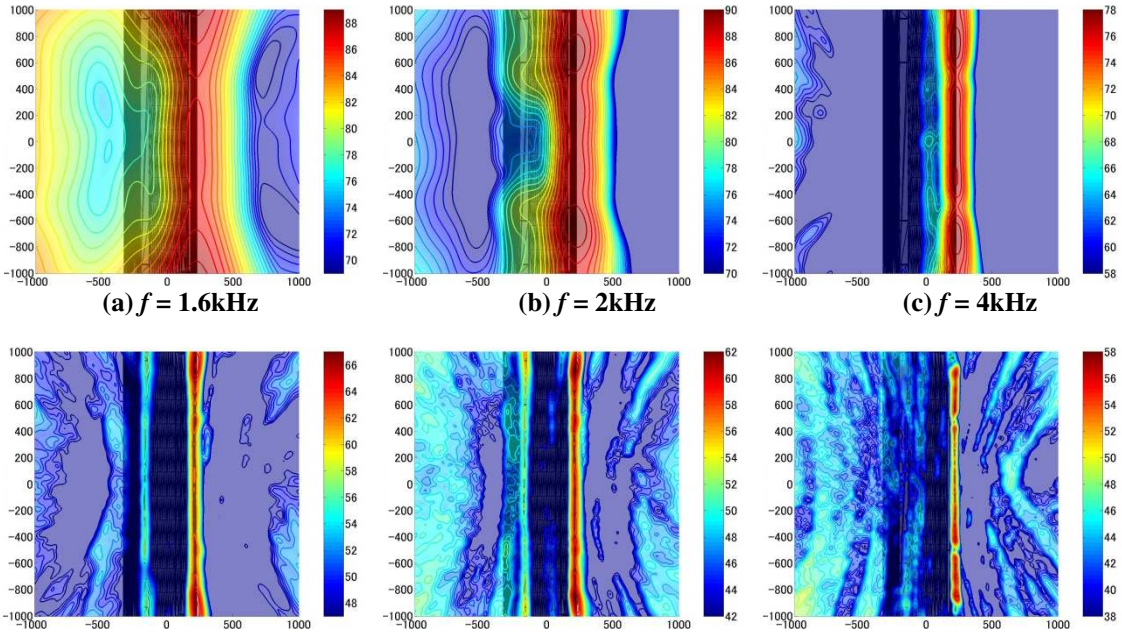

(a) f = 1.6kHz (b) f = 2kHz (c) f = 4kHz

(d) f = 8kHz (e) f = 10kHz (f) f = 16kHz

Figure 19. Phased-microphone array noise source maps (U = 58 m/s, α_u = 3.5°, contour levels correspond to SPL in one-third octave bands).

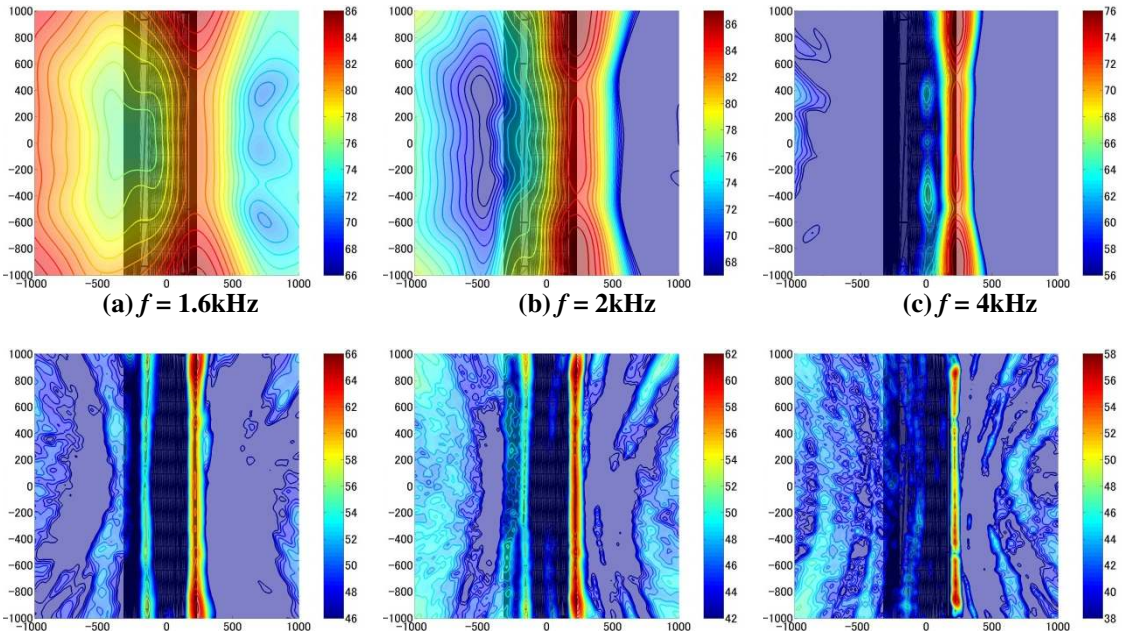

(a) f = 1.6kHz (b) f = 2kHz (c) f = 4kHz

(d) f = 8kHz (e) f = 10kHz (f) f = 16kHz

Figure 20. Phased-microphone array noise source maps (U=58m/s, α_u = 6.0°, contour levels correspond to SPL in one-third octave bands).

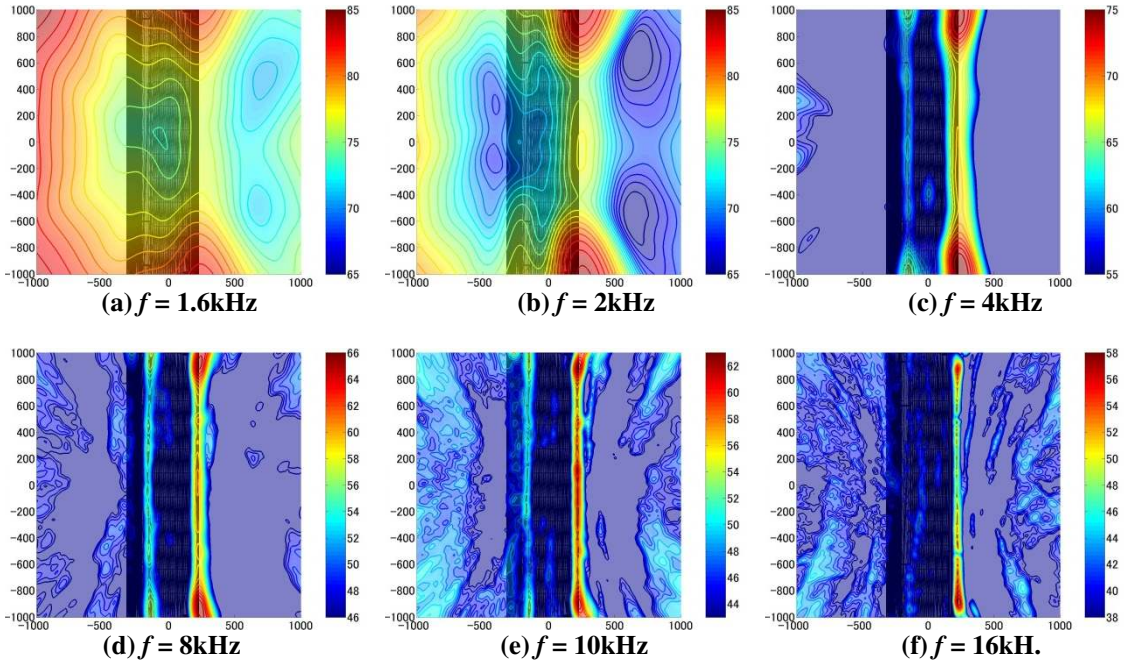

Figure 21. Phased-microphone array noise source maps (U=58m/s, α_u = 10.0°, contour levels correspond to SPL in one-third octave bands).

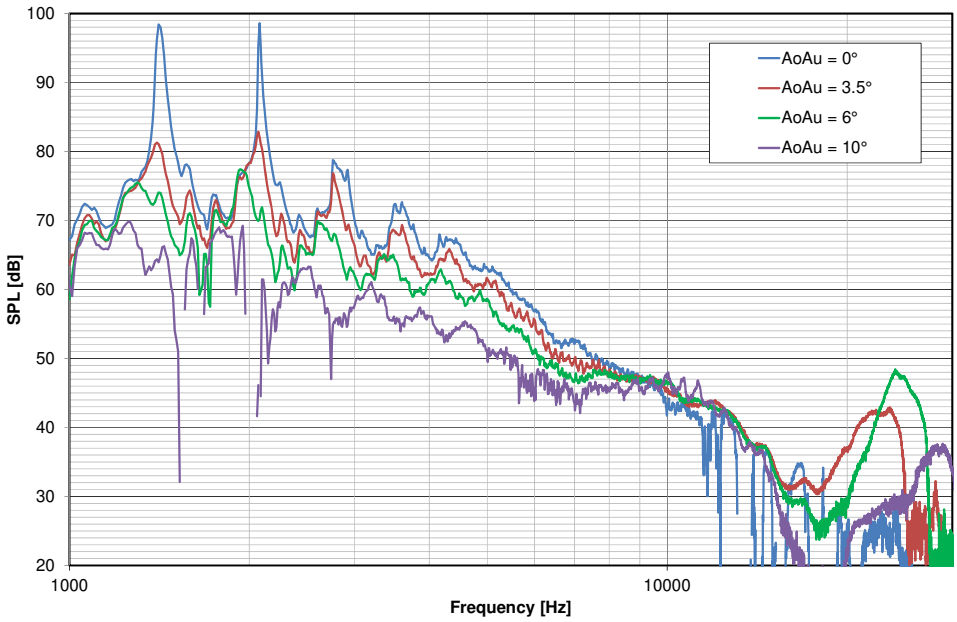

Figure 22. Acoustic spectra obtained by integrating noise source maps within SD3 at selected angles of attack (spectral bin width = 10 Hz).

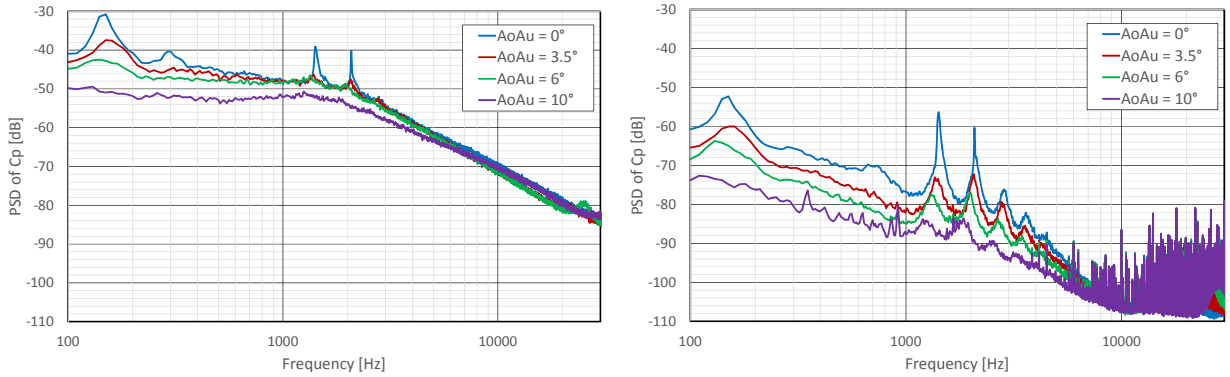

(a) Sensor S3 **(b) Sensor S10**

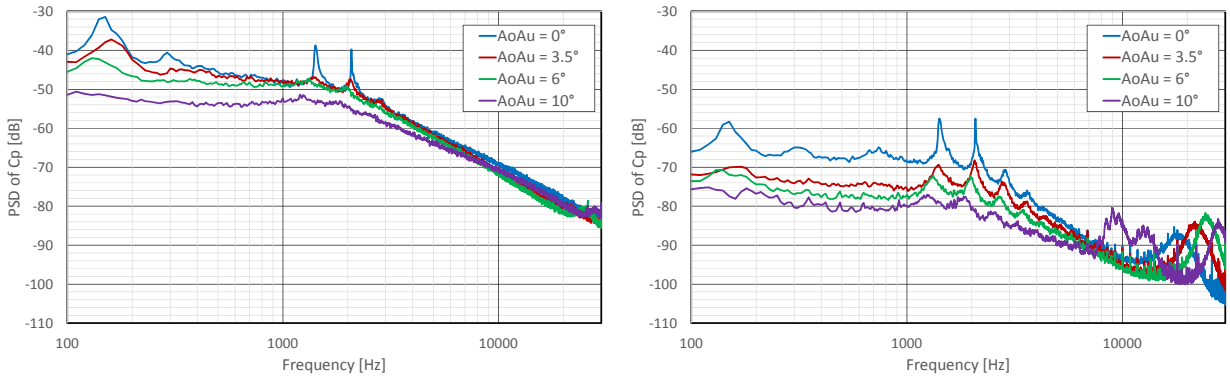

(c) Sensor S11 **(d) Sensor S13**

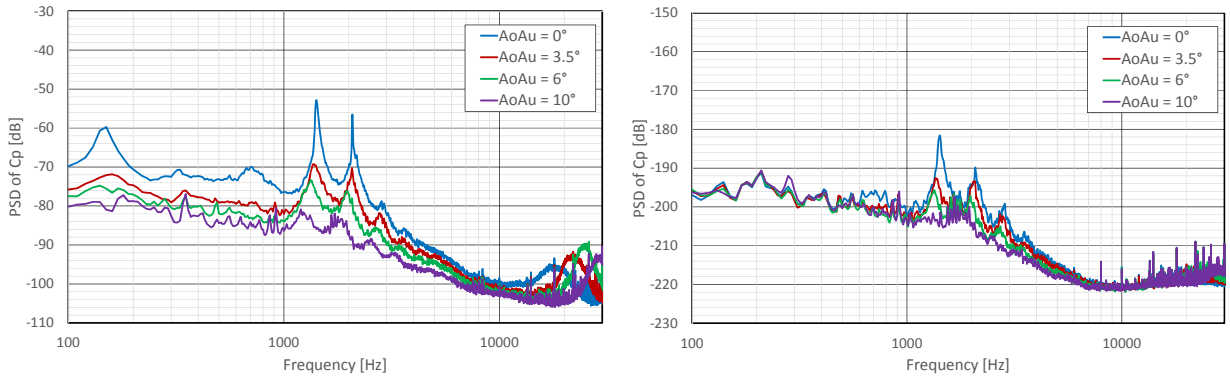

(e) Sensor M7 **(f) Sensor F1**

Figure 23. Comparison of unsteady pressure spectra based on Kulite™ measurements at selected angles of attack.

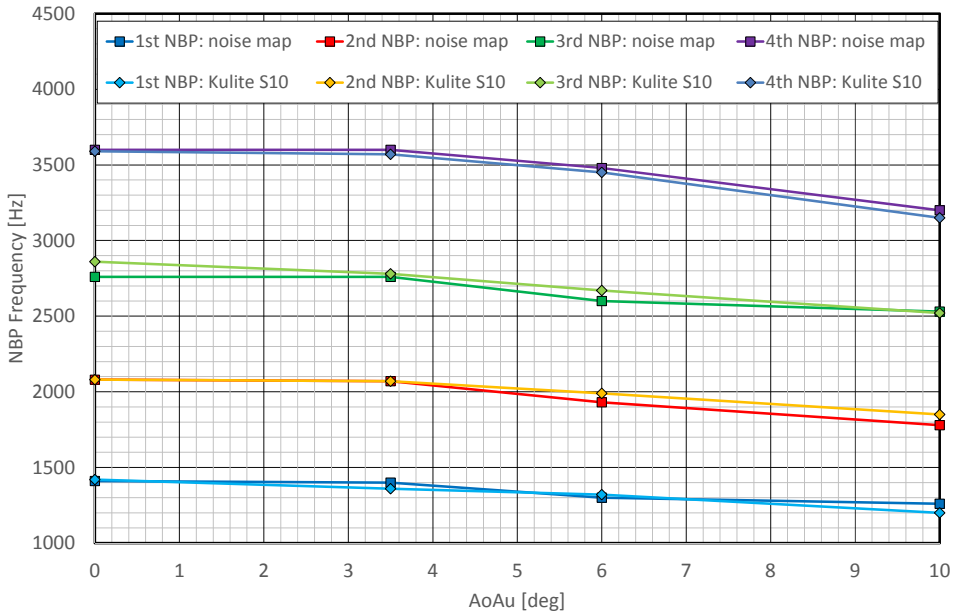

Figure 24. NBP frequencies associated with slat cove dynamics as separately estimated from the integrated spectra of noise source maps within SD3 and the spectra of Kulite™ transducer S10.

Coherence characteristics of unsteady pressure fluctuations along the model surface were also examined to assess the correlation between unsteady aerodynamic phenomena at multiple locations. Coherence was calculated using the following equation;

$$Coh^2(f) = \frac{\left|S_{XY}(f)\right|^2}{S_{XX}(f)S_{YY}(f)} \tag{1}$$

where $S_{XY}(f)$ is the cross-spectrum function between the unsteady pressure at two locations, X and Y. S_{XX}, S_{YY} are the auto-spectrum functions at X and Y. and the value of Coh^2 can range from 0 to 1. A large value of coherence implies that fluctuations at the frequency of interest are strongly correlated between X and Y. The numbers of the data points and averaging were 8192 and 50, respectively, and the sampling frequency was 81.92 kHz.

Figure 25 shows the coherence spectra for two pairs of Kulite™ transducers along the slat and the main wing, respectively. For each pair, the reference transducer is located at the spanwise location of z = -3.9624 mm (transducer S3 for the pair located on the slat and M7 for the pair on the main wing) and the other transducer is located at z = 0 (transducers S5 and M8, respectively). Figure 26 shows the coherence spectra for the sensors that were farthest apart on the slat (S11) and the main wing (M1). Because there was only one Kulite™ transducer over the flap surface, the present measurements do not provide any information about the spanwise coherence over the flap surface. For the Kulite™ transducers mounted over the slat, the spanwise coherence had large values at the frequencies corresponding to the NBPs. This behavior was first noted using computational simulations in Ref. 11. The additional NBP in the coherence spectrum at approximately 150 Hz was caused by the wind tunnel fan. At frequencies sufficiently farther from the NBP (i.e., within the purely broadband portion of the spectrum), the coherence dropped to values that were generally less than 0.2. There was a small decrease in the coherence as the angle of attack was increased from α_u = 0° to +10°, similar to the corresponding variation in the PSD levels of pressure fluctuations over the slat. Analogous to the latter trend, the coherence peak associated with vortex shedding from the slat trailing edge (f ≈ 20 kHz) is seen to become stronger as the angle of attack is increased.

The main wing transducers have a coherence of greater than 0.8 for all frequencies up to 6 kHz, indicating a stronger coherence than the selected pair of transducers over the slat. Although not shown, the coherence over the main wing remained strong even when the angle of attack was varied from 0° to +6°. Thus, the unsteady pressure field on the main wing remained nearly two-dimensional even as the coherence of the unsteady pressure field on the slat decreased significantly as the angle of attack was increased from 0° to +6°. These differences are primarily

related to the nature of pressure fluctuations measured by the two pairs of sensor. The sensors along the slat surface are exposed to strong vortical (i.e., shorter scale) fluctuations associated with shear layer strcutures whereas the sensors on the main wing are only exposed to the larger scale acoustic fluctuations emanating from the slat cove region (i.e., besides any intrinsic fluctuations within the boundary layer, which is expected to be laminar at this location).

Figure 27 shows the coherence distribution at selected frequencies as a function of spanwise probe separation at selected chordwise locations along the slat and the main wing for $\alpha_u = 0°$ to +7°. Figure 28 shows the effect of angle of attack on the reattachment location as estimated from the results of two-dimensional steady-state RANS CFD calculations. The reattachment line moves progressively upstream when the angle of attack is increased. A similar observation was made in Fig. 2(b) of Ref. 12, which was based on time accurate simulations. The angle of attack for which the predicted reattachment location coincides with the location of the spanwise array of Kulite™ pressure transducers is between α = 3° - 4°. Figures 27(a) and 27(b) show that, for all but sufficiently small probe separations, the coherence at the first two NBPs decreases rapidly as α is increased from 0° up to some critical value ($\alpha_u \approx 2.5°$) after which the coherence remains quite small at all larger angles of attack. In contrast, Figs. 27 (c) and (d) indicate that the pressure fluctuations along the main wing have a substantially larger coherence length than those along the slat. Significant coherence is noted even for probe separations of 50 mm to 100 mm along the main surface. The spanwise coherence length of the fluctuations along the main wing also decreased as α_u was increased from 0° to 2.5°, and the coherence values became rather small for $\alpha_u > 2.5°$.

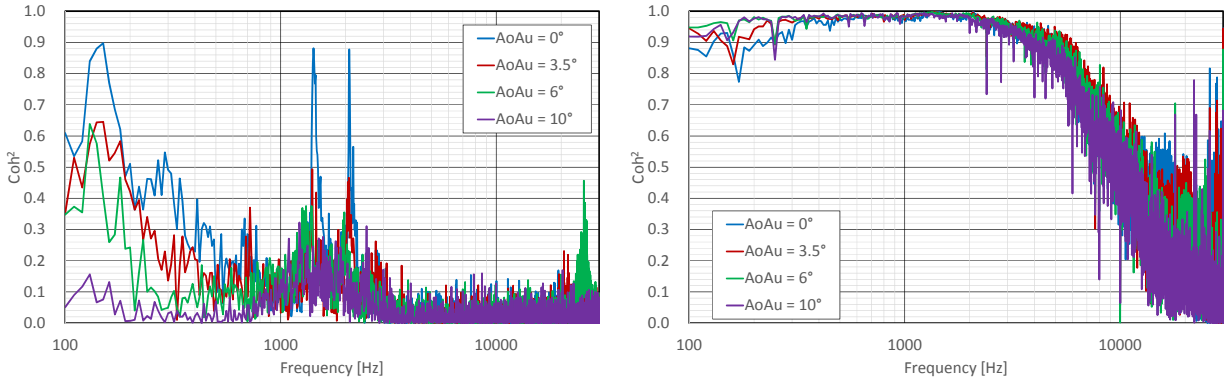

(a) Coherence: S5 – S3 **(b) Coherence: M8 – M7**

Figure 25. Coherence between reference sensors S3 and M7 at z = -3.9624 mm and the sensors along the mid-span section (z = 0 mm) of the slat (S5) and main wing (M8).

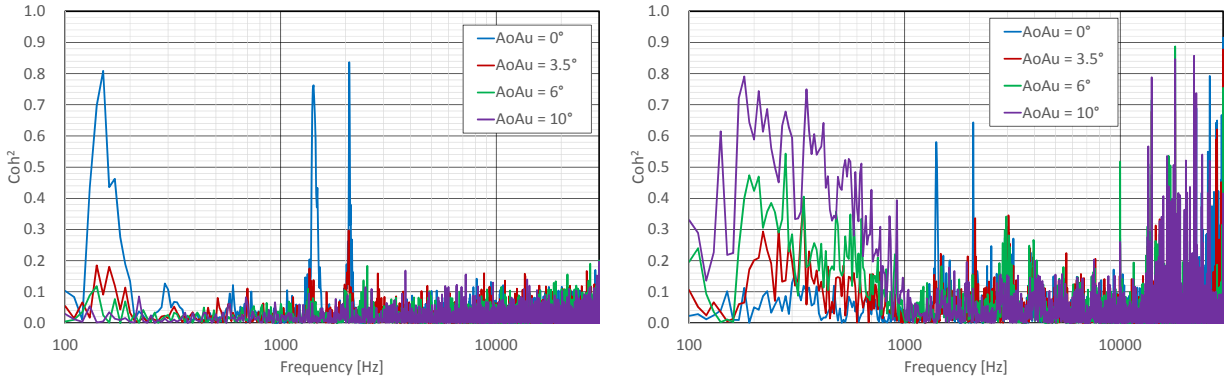

(a) Coherence S11 – S3 **(b) Coherence M1 – M7**

Figure 26. Coherence between reference sensors S3 and M7 at z = -3.9624 mm and sensors S11 and M1, respectively. The latter sensors were the farthest apart from the reference sensors on the slat and the main wing.

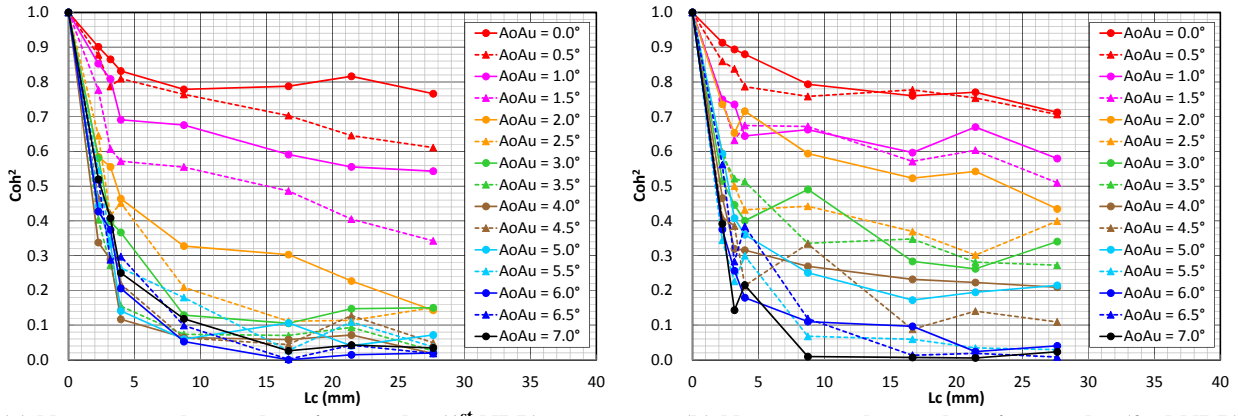

(a) Near reattachment location on slat (1st NBP) **(b) Near reattachment location on slat (2nd NBP)**

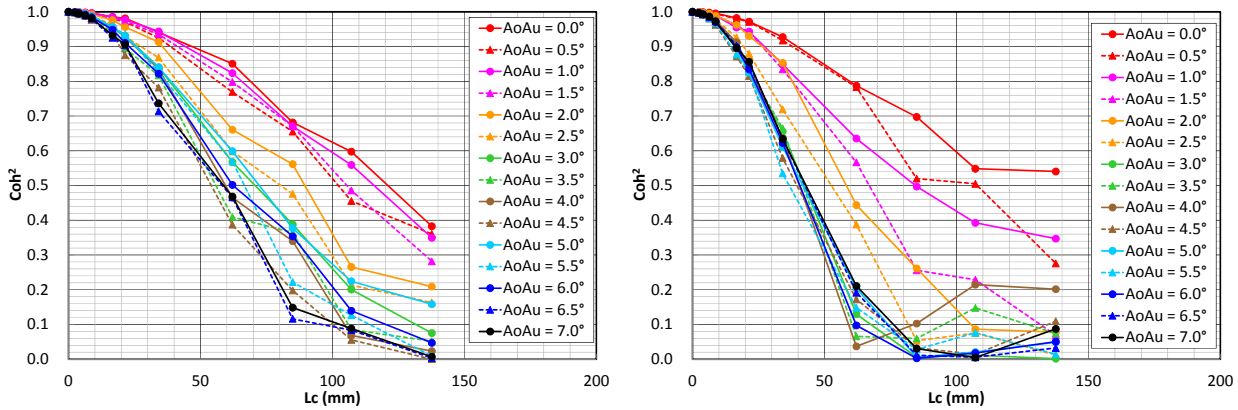

(c) Leading edge region of main wing (1st NBP) **(d) Leading edge region of main wing (2nd NBP)**

Figure 27. Coherence distribution of surface pressure fluctuations at selected narrow band peaks as a function of probe separation (U_∞ = 58 m/s).

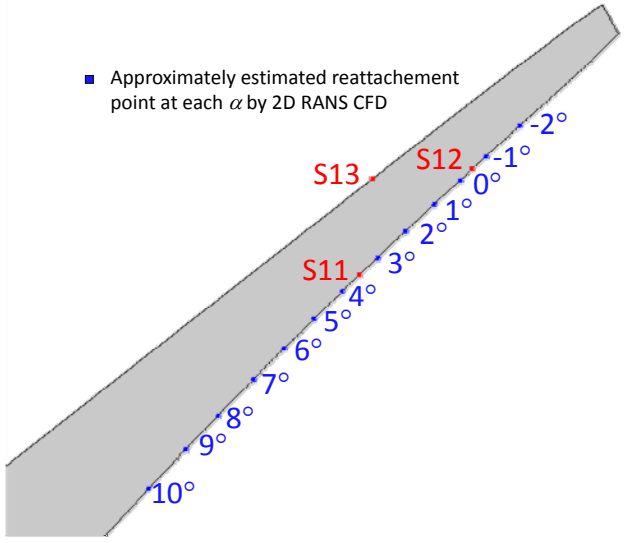

Figure 28. Effect of angle of attack on the location of the reattachment point as estimated using the results of two-dimensional steady-state RANS CFD calculations.

C. Dependence on Free-stream Velocity

Dependence of the slat noise spectra on the freestream velocity was investigated by using the 30P30N configuration without any boundary layer trips. Figures 29-31 compare the microphone phased-array spectra obtained by the integration of noise source maps within SD3 for free-stream velocities of 58 m/s, 45 m/s, and 35 m/s at the fixed angle of attack of α_u = 0°, 6°, and 10°. In both plots, the frequencies have been scaled to a freestream velocity of 58 m/s by assuming the relevant non-dimensional frequency parameter to the Strouhal number $St = f U_\infty/c$. Additionally, the SPL has been scaled using $U_\infty^{4.5}$ velocity scaling law for the intensity of slat noise.[24] At both angles of attack included in Figs. 29-31, the above rescaling for the horizontal and vertical axes leads to a reasonable collapse of the frequency and the level of NBPs. However, for f > 5 kHz, the trend in spectral levels with the flow speed is reversed, indicating that an exponent of less than 4.5 may be appropriate at the higher frequencies. Unfortunately, there is no way to independently control the Reynolds number and Mach number parameters in LWT2; therefore, the effects of one parameter cannot be easily separated from those of the other. As the flow speed is reduced from U_∞ = 58 m/s to 45 m/s, the high frequency peak associated with vortex shedding from the slat trailing edge shifts from approximately 24 kHz to 17 kHz. This variation is consistent with a purely hydrodynamic scaling (i.e., constant Strouhal number) for the shedding peak as seen from Fig. 30(b). However, this peak becomes relatively weaker as the flow speed (i.e., Reynolds number) is reduced, and no prominent peak at the corresponding Strouhal number is observed at the lowest flow speed of U_∞ = 35 m/s.

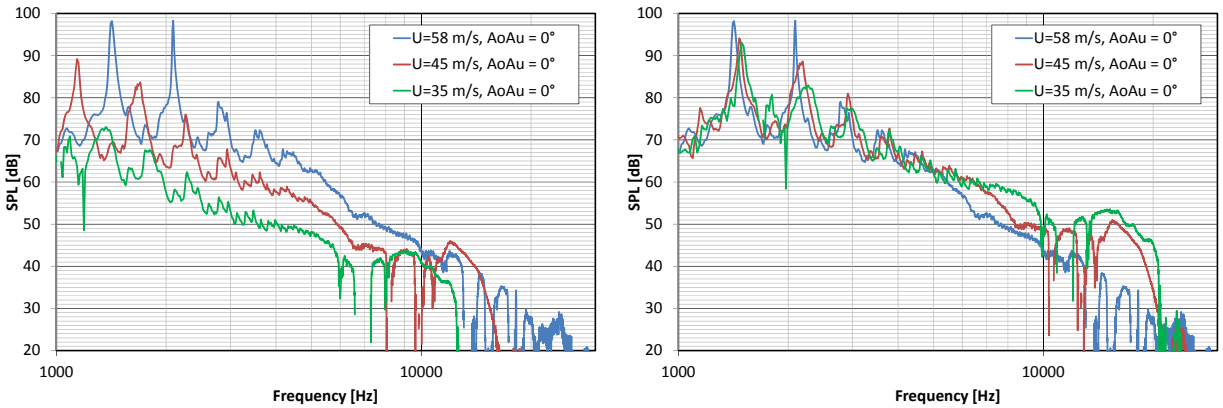

(a) No-scaling **(b) 4.5 power law scaling**

Figure 29. Comparison of microphone phased-array based acoustic spectra obtained by integration of noise source maps within SD3 at different free-stream velocities at α_u = 0° (spectral bin width = 10 Hz).

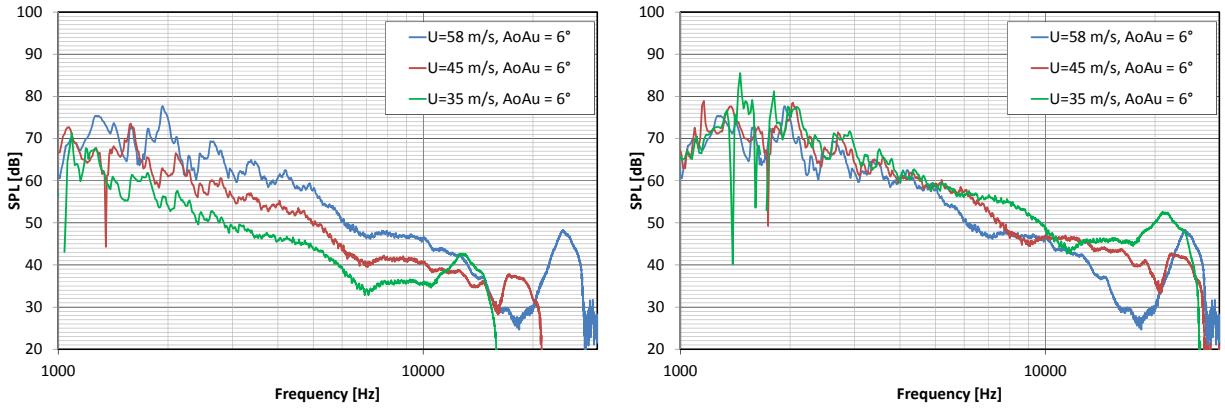

(a) No-scaling **(b) 4.5 power law scaling**

Figure 30. Comparison of microphone phased-array based acoustic spectra obtained by integration of noise source maps within SD3 at different free-stream velocities (α_u = 6°, spectral bin width = 10 Hz).

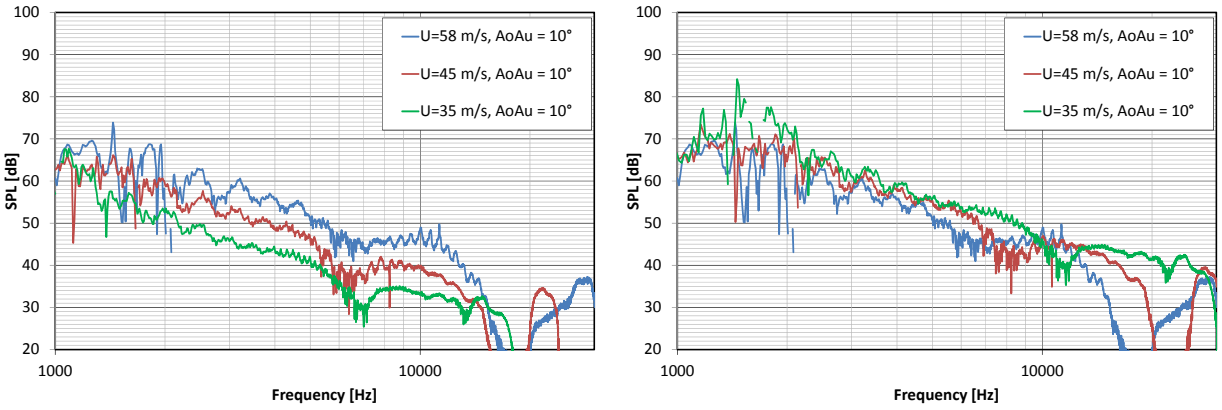

(a) No-scaling **(b) 4.5 power law scaling**

Figure 31. Comparison of microphone phased-array based acoustic spectra obtained by integration of noise source maps within SD3 at different free-stream velocities (α_u = 10°, spectral bin width = 10 Hz).

D. Effect of Boundary-Layer Trips on NBPs

Effect of boundary-layer trips on the NBPs was evaluated. Figure 32 shows the trip dots on the lower surface of the slat at a chord location between the stagnation point and the slat cusp at x/c_{slat} = 0.11. Figure 33 illustrates the effect of these trips by comparing the spectra based on the integration of noise source maps over the mid-span region of the slat, S3, at the fixed tunnel speed of U_∞ = 58 m/s. The baseline trip configuration corresponds to trip dots with 0.290 mm height on the lower surface of the main wing at 20% chord location. In two other trip configurations, trip dots of different heights, 0.152 mm and 0.218 mm were employed on the lower surface of the slat at x/c_{slat} = 0.11. In the latter two configurations, the trip dots along the lower surface of the main wing were the same as the first, i.e., baseline trip configuration. For the all trip dots, the diameter of the dots was equal to 1.27 mm and the spacing between the centers of each pair of adjacent dots was equal to 2.54 mm. Because the data with 0.152 mm roughness height was not obtained at α_u = 6°, the comparison is conducted using the results at α_u = 0°, 5°, and 10°. At both trip heights, the presence of trip dots along the slat surface led to a considerable increase in the level of the NBPs at α = 0° and 5°. With the exception of the first NBP near 1.4 kHz at α = 0°, the increase in NBPs was nearly the same for both heights of the trip dots used on the slat surface. At α_u = 10.0° where the levels of NBPs were originally much lower, the presence of trip dots had very little effect on the noise spectra.

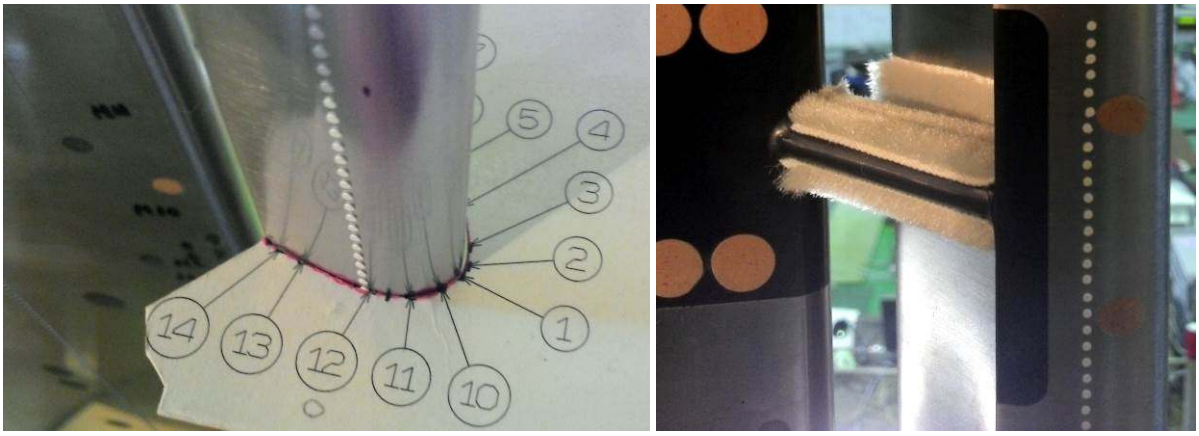

Figure 32. Trip dots on the lower surface of the slat at a chord location between the stagnation point and the slat cusp at x/c_{slat} = 0.11. The array of dots is labeled as 12 in the figure.

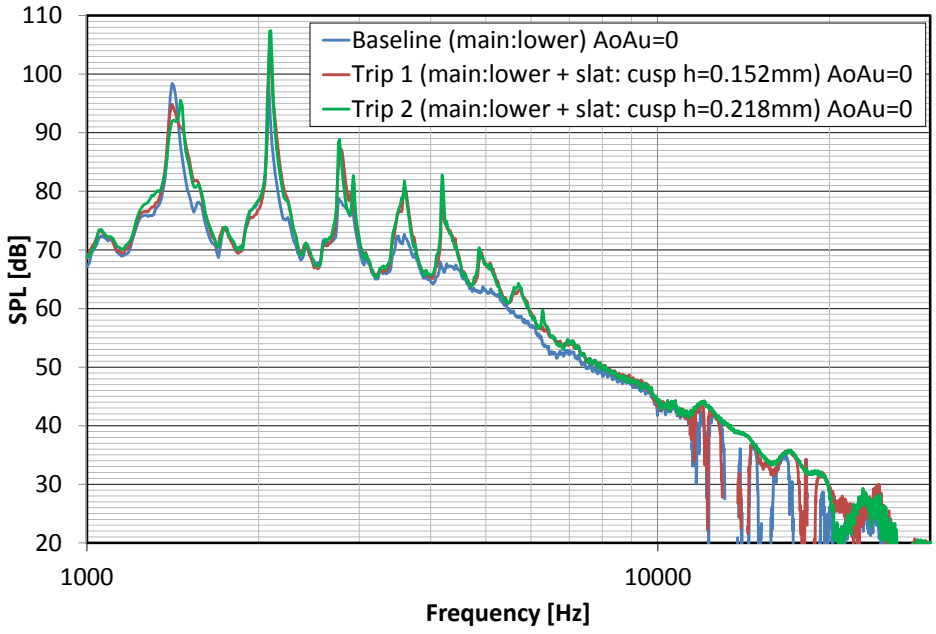

(a) α_u = 0.0°

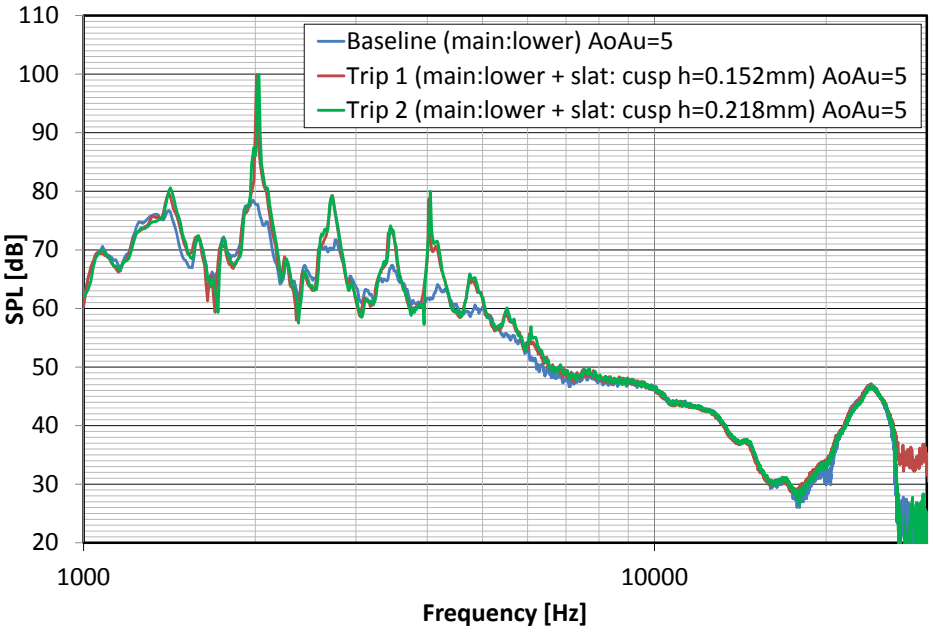

(b) α_u = 5.0°

Figure. 33 Effect of boundary layer trips on microphone phased-array based acoustic spectra obtained by integration of noise source maps within SD3 at U_∞ = 58 m/s (spectral bin width = 10 Hz). (continued)

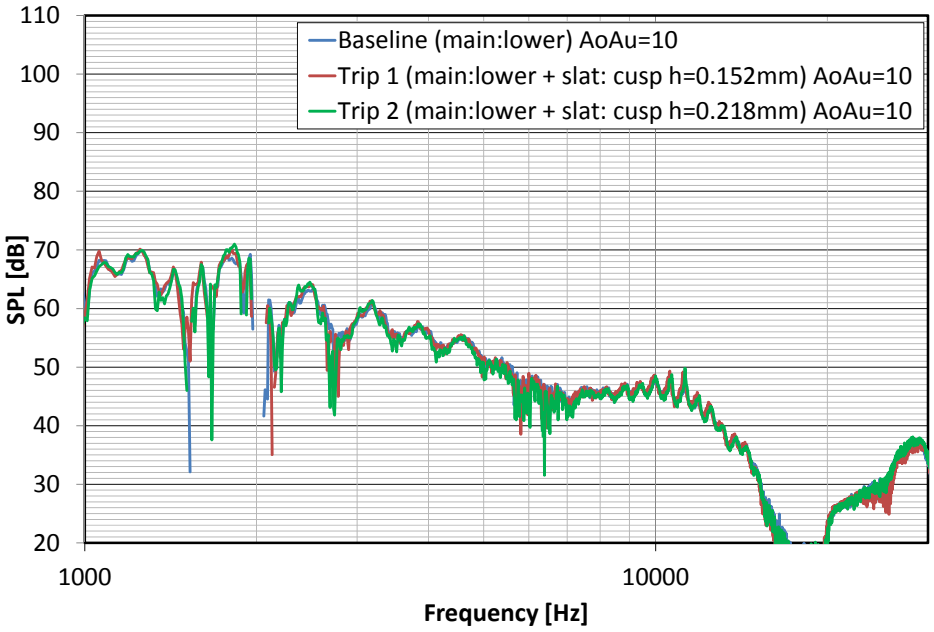

(c) α_u = 10.0°

Figure 33. Effect of boundary layer trips on microphone phased-array based acoustic spectra obtained by integration of noise source maps within SD3 at U = 58 m/s. (spectral bin width = 10 Hz). (concluded)

IV. Summary and Concluding Remarks

Aeroacoustic measurements associated with noise radiation from the leading edge slat of the canonical, unswept 30P30N three-element high-lift airfoil configuration have been obtained in a 2m × 2m hard-wall wind tunnel at the Japan Aerospace Exploration Agency (JAXA). Obtained as part of an ongoing collaboration with NASA Langley Research Center, these measurements are designed to provide an important component of the dataset for Category 7 of the AIAA workshops on Benchmark problems for Airframe Noise Computations (BANC) and, more generally, an improved understanding and characterization of the noise source mechanisms associated with a leading edge slat under conditions that are relevant to landing approach. The first phase of these measurements reported in this paper was focused on obtaining reliable near-field data with quasi-two-dimensional near-field characteristics. The acquired data included static and dynamic pressure measurements (including auto-spectra and spanwise coherence) and qualitative acoustics maps based on a phased array of microphones within a closed, hard-wall test section.

The main findings of this study may be summarized as follows:

1. For an angle of attack up to 10 degrees, the mean surface *Cp* distributions agree well with free-air two dimensional CFD predictions corresponding to a corrected angle of attack with the exception of a small difference between the CFD and the measurement in regard to flow separation near the trailing edge on the upper surface of the slat. The nearly constant 0.5 degree correction is believed to be caused by the extra downwash caused by sidewall flow separation along the flap surface.
2. The surface pressure spectra as well as the acoustic spectra associated with slat cove dynamics exhibit a mix of broadband component and narrow-band peaks. Both components become progressively weaker as the angle of attack is increased from 0 to 10 degrees. The frequencies of narrow-band peaks change little from α_u = 0° to α_u = 3.5°; however, decrease by approximately 10 percent across the range α_u = 3.5° to α_u = 10°. The peak frequencies at a fixed angle of attack exhibit an approximate Strouhal number scaling, with a weak dependence of the Strouhal number on the flow speed. The spanwise coherence of surface pressure fluctuations near the reattachment location of slat surface as well as near the leading edge of the main wing decreases rapidly with increasing angle of attack when α_u is small; however, the dependence on α_u becomes significantly weaker at the large angles of attack. The presence of trip dots between the stagnation point and slat cusp is found to result in significantly enhanced levels of narrow-band peaks in the acoustic spectra inferred from phased microphone array measurements. However, the frequencies corresponding to these peaks remain unchanged within the resolution of the measurement.

The measurements presented herein provide a significant body of information concerning the frequencies, fluctuation intensities, and spanwise coherence characteristics of the narrow-band peaks as well as their variation with the angle of attack, flow speed, and the state of the boundary layer. Unfortunately, the causality of these narrow band peaks cannot be established on the basis of measurements presented herein. However, a combination of these results and detailed simulations along with PIV and unsteady PSP measurements should help bridge this gap within the near future.

Acknowledgments

The authors would like to thank Mr. Douglas Weber and Mr. Christopher Cagle at NASA Langley Research Center and Mr. Hiroshi Uchida, Mr. Takayuki Kato, Mr. Shigemi Shindo, Mr. Tohru Hirai, Mr. Kentaro Tanaka, and Dr. Kazuhisa Amemiya at JAXA for their assistance with the hardware design of the modified slat model and wind tunnel testing.

References

1. Astley, J., "Predicting and Treating Fan and Turbomachinery Noise Current Technology, Research & Facilities," UK-Japan Bilateral Workshop (Aircraft Emissions and Noise), Tokyo, 2006.
2. Hardin, J. C., "Airframe self-noise: Four Years of Research; Aircraft Noise Reduction for Commercial Aircraft," NASA-TM-X-73908, 1976.
3. Dobrzynski, W., "Almost 40 Years of Airframe Noise Research: What Did We Achieve?," *Journal of Aircraft*, Vol. 47, No. 2, 2010.
4. https://info.aiaa.org/tac/ASG/FDTC/DG/BECAN_files_/BANCII_category7/Summary_Category_7_Slat_Noise_30P30N.pdf (March 2014).
5. Choudhari, M. and Yamamoto, K., "Integrating CFD, CAA, and Experiments towards Benchmark Datasets for Airframe Noise Problems," Proceedings of 5th Symposium on Integration CFD and Experiments in Aerodynamics (Integration 2012), October 2012.
6. Rudnik, R., and Geyr, H., "The European High Lift Project EUROLIFT II – Objectives, Approach, and Structure," AIAA Paper 2007-4296, 2007.
7. Rumsey, C.L., Long, M., Stuever, R. A., and Wayman, T. R., "Summary of the First AIAA CFD High Lift Prediction Workshop," AIAA Paper 2011-0939, 2011.
8. Murayama, M., Yokokawa, Y., Yamamoto, K., and Ueda, Y., "CFD Validation Study for a High-Lift Configuration of a Civil Aircraft Model," AIAA Paper 2007-3924, 2007.
9. https://info.aiaa.org/tac/ASG/FDTC/DG/BECAN_files_/BANCII.htm (May 1, 2014).
10. Klausmeyer, S. M. and Lin, J., "Comparative Results from a CFD Challenge Over a 2D Three-Element High-Lift Airfoil," NASA TM 112858, 1997.
11. Lockard, D. P. and Choudhari, M. M., "Noise Radiation from a Leading-Edge Slat," AIAA Paper 2009-3101, 2009.
12. Choudhari, M. M., Lockard, D. P., Khorrami, M. R., and Mineck, R. E., "Slat Noise Simulations: Status and Challenges," Proceedings of Inter-Noise 2011, ed. Hiroyuki Imaizumi, Osaka, Japan, Sept. 4-7, 2011.
13. Yokokawa, Y., Imamura, T., Ura, H., Ito T., Uchida, H., and Yamamoto, K., "Studies on Airframe Noise Generation at High-lift Devices in Relation to Aerodynamic Performances," AIAA Paper 2008-2960, 2008.
14. Imamura, T., Ura, H., Yokokawa, Y., Hirai, T., Yamamoto, K., "Numerical and Experimental Research of Low-Noise Slat Using Simplified High-lift Model," AIAA Paper 2008-2918, 2008.
15. Imamura, T., Yokokawa, Y., Ura, H., and Yamamoto, K., "A Far-field Noise and Near- field Unsteadiness of a Simplified High- lift- configuration Model (Slat)," AIAA Paper 2009-1239, 2009.
16. Yokokawa, Y., Murayama, M., Ito, Y., Ura, H., Kwak, D., Kobayashi, H., Shindo, S., and Yamamoto, K., "Noise Generation Characteristics of a High-lift Swept and Tapered Wing Model," AIAA Paper 2013-2062, May 2013.
17. Ito, T., Ura, H., Nakakita, K., Yokokawa, Y., Ng, F., W., Burdisso, A., R., Iwasaki, A., Fujita, T., Ando, N., Shimada, N., and Yamamoto, K., "Aeroacoustic testing in Anechoic Closed Test Sections of Low-speed Wind Tunnels," AIAA Paper 2010-3750, 2010.
18. Yamamoto, K., Ura, H., Yokokawa Y., Imamura, T., Nakakita, K., Camargo, H., Remillieux, M., Boor, Z., Burdisso, A. R., Ng, F. W., Uchida, H., and Ito., T., "Aeroacoustic Testing of a High-Lift Device Model in the Virginia Tech Anechoic Wind Tunnel," Proceedings of 13th CEAS-ASC Workshop & 4th Scientific Workshop of X3 – Noise, Oct. 2009.
19. Nakakita, K., "Scanning Unsteady PSP Technique for High-Frequency and Small-Pressure Fluctuation in Low-Speed," AIAA Paper 2010-4920, 2010.
20. Johnson, D. H. and Dudgeon, D. E., "Array Signal Processing," PTR Prentice Hall, 1993.
21. Mueller, T. J. (Ed.), "Aeroacoustic Measurement," Springer, 2001.
22. Sijtsma, P., "Experimental Techniques for Identification and Characterization of Noise Sources," NLR-TP-2004-165, 2004.
23. Kolb A, Faulhaber R, Drobietz R, and Grünewald M., "Aeroacoustic Wind Tunnel Study on a Two-Dimensional High-Lift Configuration," AIAA Paper 2007-3447, 2007.
24. Pott-Pollenske, M., Alvarez-Gonzalez J., and Dobrzynski, W., "Effect of Slat Gap/Overlap on Farfield Radiated Noise," AIAA Paper 2003-3228, 2003.